

Pressure and Temperature Fields Associated with Aero-Optics Tests[†]

K.R.Raman
Raman Aeronautics, Inc.

Summary

This paper describes the experimental investigations carried out in the 6 x 6 ft Ames wind tunnel at Moffett Field, California, on four model configurations in the Aero-Optics series of tests, and presents the data obtained on the random pressures (static and total pressures) and total temperatures from these tests. In addition, the data for static pressure fluctuations on the Coelostat turret model are presented.

These measurements indicate that the random pressures and temperatures are negligible compared to their own mean (or steady state) values for the four models considered, thus allowing considerable simplification in the calculations to obtain the statistical properties of the density field. In the case of the Coelostat model tests these simplifications cannot be assumed a priori and require further investigation. Some correlation data obtained using two identical probes, are also presented here. From these correlation plots appropriate scale lengths can be determined.

Symbols

M	Free-stream Mach number	\vec{X}	Position vector, (x,y,z), L
p	Static pressure, N/m ²	θ	Angular orientation of cavity in the Coelostat turret model, deg
\tilde{p}	RMS value of static pressure, N/m ²	τ	Time delay, sec.
p_T	Total pressure, N/m ²	<u>Subscripts and Superscripts</u>	
\tilde{p}_T	RMS value of total pressure, N/m ²	∞	Free-stream conditions
PSD	Power spectral density, (N/m ²) ²	\sim	RMS value of the parameter
q	Dynamic pressure, N/m ²	$-$	Steady state value of the parameter considered
Re/m	Reynolds number per meter, 1/L	l	Local conditions
RMS	Root mean square value of parameter under consideration		
T_T	Total temperature, °K		
\tilde{T}_T	RMS value of total temperature, °K		
ΔT	Surface temperature increase of splitter plate, °K		
\vec{U}_∞	Free-stream velocity, m/sec		

[†] This reported work was carried out under contract NAS 2-9920 funded by NASA/Ames Research Center, Moffett Field, CA.

Introduction

A laser beam from an Airborne Laser Laboratory (ALL) degrades in its performance as it passes through the aerodynamic flow field shrouding the aircraft. This performance degradation is directly dependent on the refractive index variations in time and space in the media. The refractive index itself is related to the local density, a parameter not readily amenable to direct measurements. In order to obtain the density field data indirectly one needs the measurements of all the pertinent aerodynamic flow field parameters, namely, pressure (static and total pressures), temperature and velocity in the selected regions of interest. In this series of tests several experimenters participated, each contributing in his own field of expertise, and through the combined efforts a considerable amount of knowledge has been gained. The data concerning the pressure and temperature field will be discussed in this paper. Using the results from this experimental investigation along with some additional measurements of their own regarding the velocity field (using a Laser Doppler velocimeter) and the mass flux data acquired with the use of hotwire anemometry, an assessment of the density field was made by Rose and Johnson in their paper entitled "Unsteady Density and Velocity Measurements".

In addition, the information regarding scale lengths along the look direction of the pointing and tracking systems is required in order to determine the Strehl ratio along the optical path.

Experimental Facility

The wind-tunnel test facility and all the model configurations used in these tests are described fully by Buell in his paper "Overview of 6 x 6 ft Wind-tunnel Aero-Optics Tests" and in Ref.1. These tests were carried out with the following wind-tunnel test section flow conditions:

$$\begin{aligned} 0.50 < \text{free-stream Mach number, } (M_\infty) < 1.00 \\ 6 \times 10^6 < \text{Reynolds number/meter} < 10^7 \\ 290^\circ \text{ K} < \text{total temperature of test stream} < 310^\circ \text{ K} \end{aligned}$$

In fig. 1 the four models that were considered in this investigation are sketched with all significant components identified in order to point out the differences between each of the models tested.

Instrumentation

A rake consisting of 20 total pressure tubes and 2 static pressure tubes spanning 17 cm normal to the splitter plate was used to obtain the steady velocity profiles in the regions of interest. The surface static pressure[†] † Static pressures being constant through the boundary layer (verified by our measurements) is the reason for using surface static pressures in calculations.

and free-stream total temperature data were necessary in these velocity calculations from the rake pressure data.

A specially designed " multi-probe " was used to measure steady and unsteady components of static pressures, total pressures and total temperatures in the region between the splitter plate and the return mirror and in regions above the cubical cavity opening. In fig.2 details of the multi-probe are schematically illustrated. The probe contains several components, all of them labelled in the sketch and briefly described in the figure itself. Two differential pressure sensors, *I* and *II*, monitor the fluctuations in total pressures and static pressures about their local mean pressures. The electrical leads are omitted in this illustration to avoid confusion. Tube AA (sensing the total pressure) is connected to a 4 meter long small capillary tubing (diam= 0.5 mm) in order to damp all the unsteady components before it is branched into two tubes. One of the branches is connected to A'A' and thus becomes the reference pressure for sensor *I*; the other branch is connected to an appropriate sensor for obtaining the steady state total pressure. Similar procedure is adopted for the static pressure sensor *II* to obtain the fluctuations about its local mean static pressures.

A hot-wire probe is mounted ahead of the total pressure opening(see fig.2). The bent prong tips are made of Nicoll wire and the 5 microns tungsten wire is welded to these tips. The hot-wire itself is located well ahead of the pressure port in order to avoid the wake influence from the hot-wire or the tips. The frequencies present behind the wire due to vortices (assuming a Strouhal number of 0.2) that are shed are well above the operating range of the sensor *I*. For temperature measurement the hot-wire is operated at low overheating ratio and in a constant current mode of operation. Appropriate compensation electronic circuitry was built to rectify for the inherent thermal lag in the hot-wire anemometer and thus the signals from the wire itself are valid up to 10 KHz in these tests.

All required signal conditioning electronics, amplifiers for various sensors, power supplies for excitation voltages etc are standard procedure and will not be discussed in this paper. Similarly, the use of tape recorders, RMS modules, Correlators etc will not be considered here. All through the data acquisition and data analysis phases, proper calibration of the electronic units needs to be carefully made and proper records of the gains, zero offsets etc are to be kept. In all this bookkeeping of the above described electronic units, the HP-9830 desk computer has been programmed and relied on.

Results and Discussion.

The velocity profiles for models 1 and 13 are presented in fig. 3 and 4 for free-stream Mach numbers equal to 0.60 and 0.89 and Reynolds number/meter equal to 9.8×10^6 . The combination of turbulence generating pins and seeding pins in model 1 and the seeding pins alone in model 13 yield comparable boundary-layer thicknesses satisfying the power law profile with $7 \leq n \leq 9$. Thus the seeding pins alone are sufficient to generate the necessary thick

boundary layer for the series of tests considered here.

The splitter plate surface temperature was elevated above the adiabatic wall temperature by $44^{\circ} - 56^{\circ} \text{ K}$ (through heating the plate) in order to increase the total temperature fluctuations in the boundary layer and thereby bring about an increase in density fluctuations adjacent to the plate. The effects on the optics performance could then be examined. However, heating the plate did not greatly affect the velocity profiles or the unsteady pressures, so the addition of heat in these tests was inadequate to bring about the anticipated effects.

In figures 5(a) and 5(b) the normalized pressures, namely the ratios of RMS static pressure to the mean free-stream static pressure, $\tilde{p} / \bar{p}_{\infty}$, and the RMS total pressure to the mean free-stream total pressure, $\tilde{p}_T / \bar{p}_{T\infty}$, are given for model 1, $M_{\infty}=0.60$ and $M_{\infty}=0.89$ respectively. Similar data are presented in figures 6, 7 and 8 for models 2, 13 and 14. From these we note that the normalized pressures satisfy

$$0.007 < \tilde{p} / \bar{p}_{\infty} < 0.020 \quad \text{and} \quad 0.020 < \tilde{p}_T / \bar{p}_{T\infty} < 0.080$$

The measurement of unsteady total temperature as obtained by hot-wire anemometer in a constant current operation are given in figures 9, 10, 11 and 12 for $M_{\infty}=0.60$ and $M_{\infty}=0.89$ for all the four models considered. The essential features to observe from these measurements are

i) the surface heat addition to the splitter plate did not greatly influence the ratios of the RMS total temperatures to the free-stream total temperatures, $\tilde{T}_T / \bar{T}_{T\infty}$, and

ii) the ratio of $\tilde{T}_T / \bar{T}_{T\infty}$ in all cases considered is less than 1%.

Using two identical multi-probes as illustrated in figure 13, and varying the separation distance between these two probes (in our investigation the normal distance to the splitter plate was varied), various cross-correlation functions were obtained. From these the scale lengths were extracted for each of the flow parameters under investigation.

In figs. 14(a), (b), and (c) the cross-correlation functions are given for static pressure, total pressure and total temperature respectively for model 1, $M_{\infty} = 0.89$. Similar plots are given for model 13, $M_{\infty} = 0.89$, in figs. 15(a), (b), and (c). The correlation scale lengths obtained for static pressure in general are greater than that for total pressures or total temperatures. The solid curves in these correlation plots were obtained by assuming an exponential form for the decay with increasing d and using a least square fit analysis. From this analysis the integral scale lengths are deduced. Further, if the hot-wire frequency range could be improved beyond 10 kHz, the scale length obtained from the total temperatures is expected to be comparable to the scale lengths obtained for total pressures (the pressure sensor frequency range is beyond 20 kHz).

During these tests the cross correlation functions involving fluctuations of static pressures, p , mass flux, ρu , total pressure, p_T , and total temperatures, T_T , were observed. The results indicate these correlations to be nearly zero; that is, $\overline{p(\rho u)}$, $\overline{pp_T}$, $\overline{pT_T}$ and $\overline{p_T T_T}$ are nearly zero. Thus the influence of these quantities in their contribution to RMS density values could be ignored.

In figure 16, the ratio of RMS static pressures to the local steady static pressures on the Coelostat turret model is plotted as a function of X distance. As can be seen in this case, the \tilde{p}/\bar{p}_1 can be as large as 8% and can play a major role in the RMS density calculations. In figure 16 the pressure data are indicated by A, B, C, D and E and correspond to sensors on the turret itself (A, B & C) and on the splitter plate (D & E). These are designated in order to present data of the power spectral analyses in figures 17 and 18 corresponding to these sensors. The pressure ports A and C are located on each side of the pressure sensor B in the cavity itself. Pressure sensors D and E are located downstream of the turret model.

In figures 17 and 18 the frequency content of the unsteady pressures corresponding to the sensors A to E (as given in figure 16) are presented. These power spectral density analyses were carried out at Ames Research Center using an existing Hybrid Spectral Analyzer program. In these plots the power spectral density peaks appearing at 1 kHz are due to the wind tunnel itself while the peaks at 500 Hz are due to flow associated with the Coelostat Turret model. Sensor C located on one side of the cavity does not show the peak at 500 Hz while the sensor A on the other side of the cavity shows the peak in the spectral plots. The influence of these peak signals downstream of the turret model is apparent from the results given in figure 18. As expected there is a high degree of coherence between the pressures between A, B, D and E sensors and slightly lower coherence value whenever sensor C was involved.

Reference

1. Buell, Donald A. Aerodynamic Properties of a Flat Plate with Cavity for Optical-Propagation Studies. Jan 1979. NASA Tech.Memo. 78487.

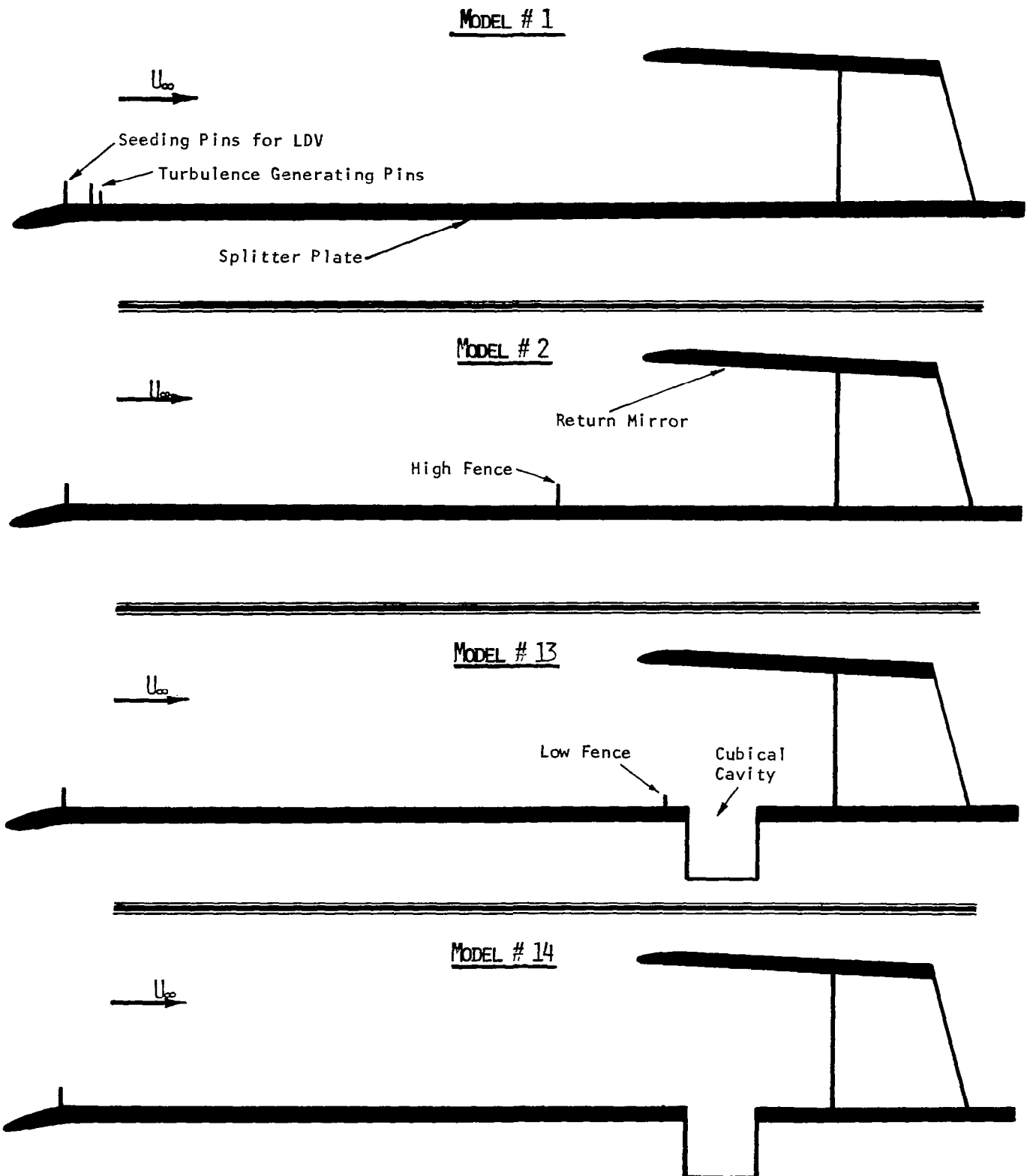


Figure 1. Sketch of the Four Selected Models Tested in 6x6 Foot Wind Tunnel.

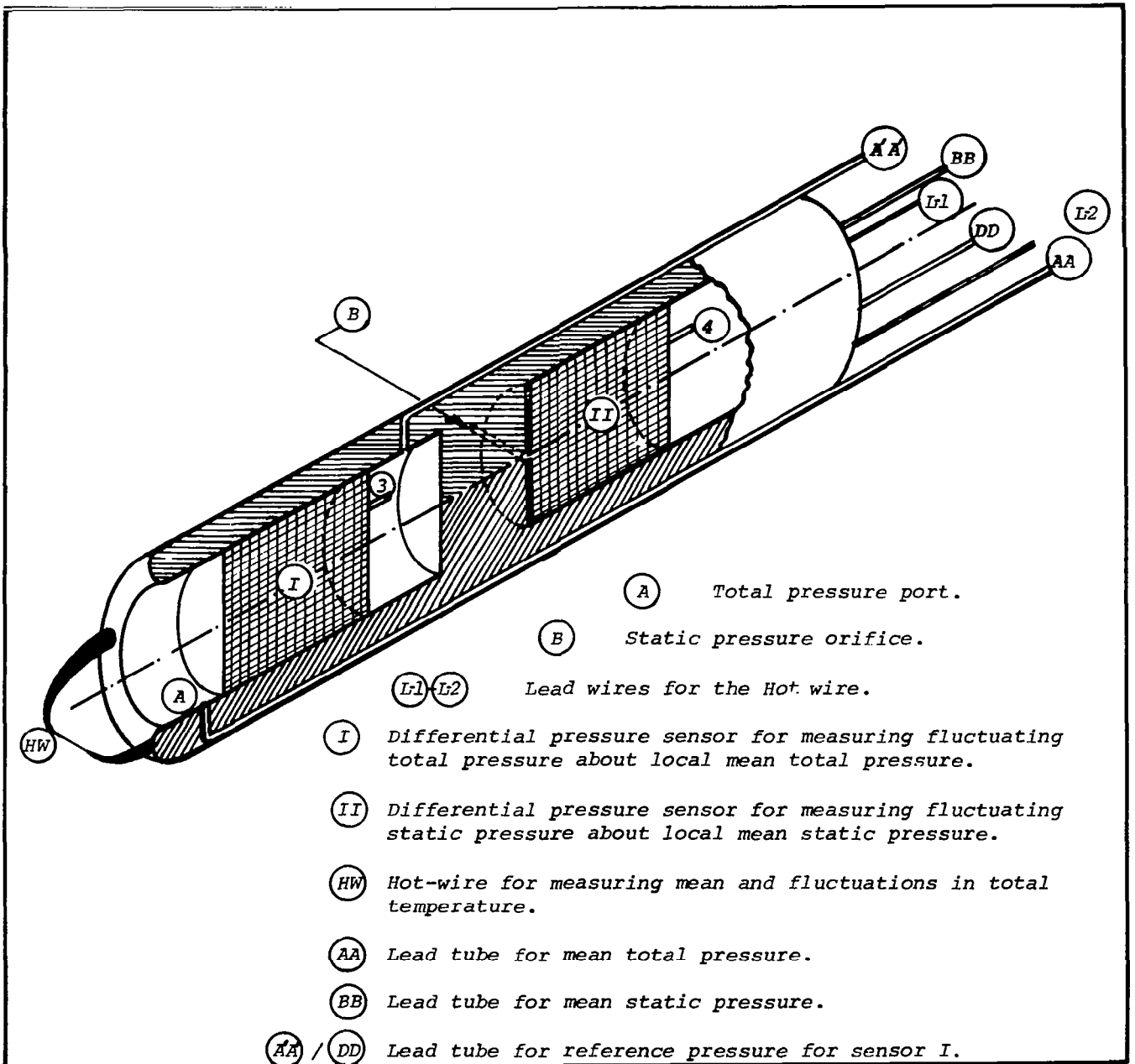


Figure 2. Details of the Multi-probe Schematically Illustrated.

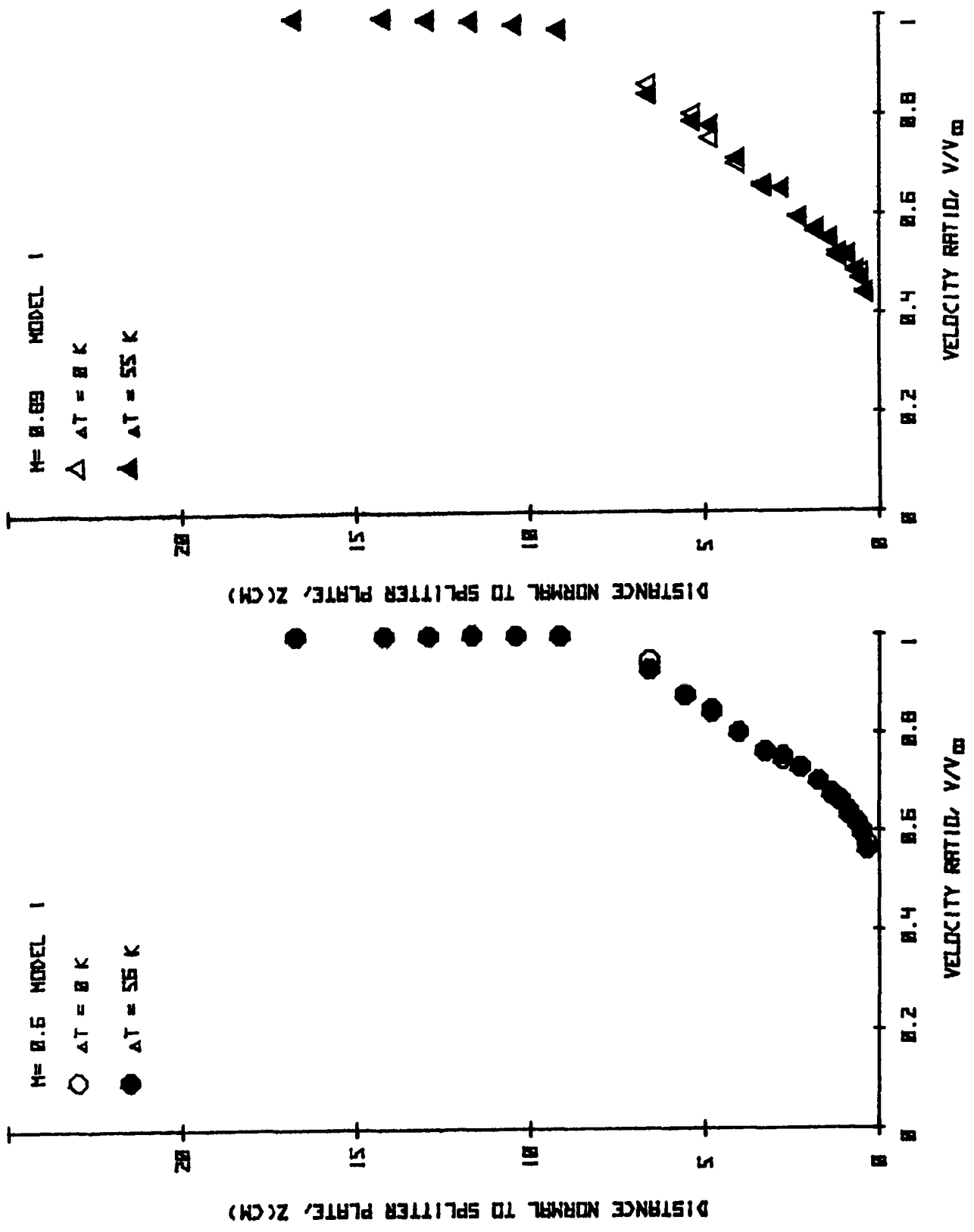


Figure 3. Velocity Profiles for Model 1 for Free-stream Mach Number 0.60 and 0.89.

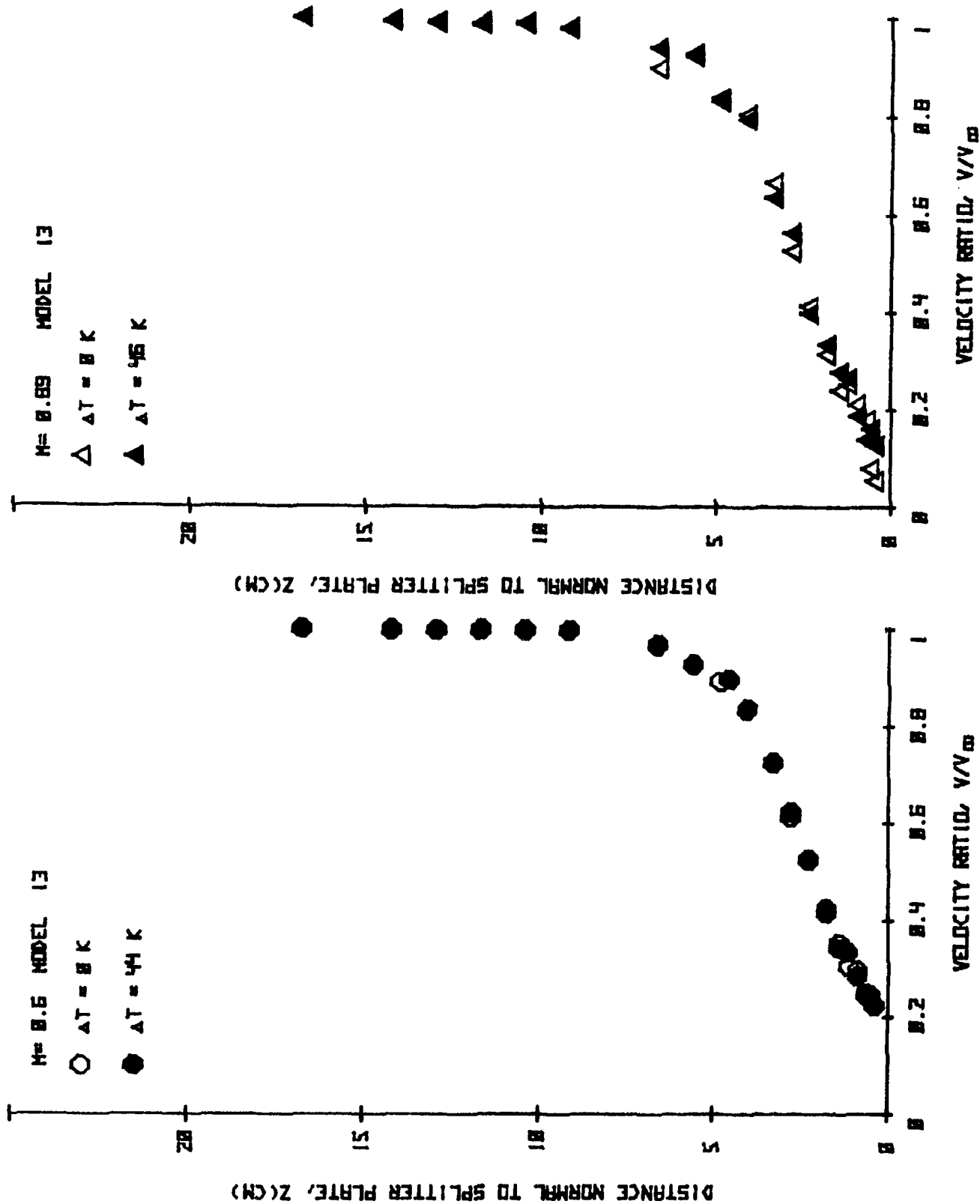


Figure 4. Velocity Profiles for Model 13 for Free-stream Mach Numbers 0.60 and 0.89.

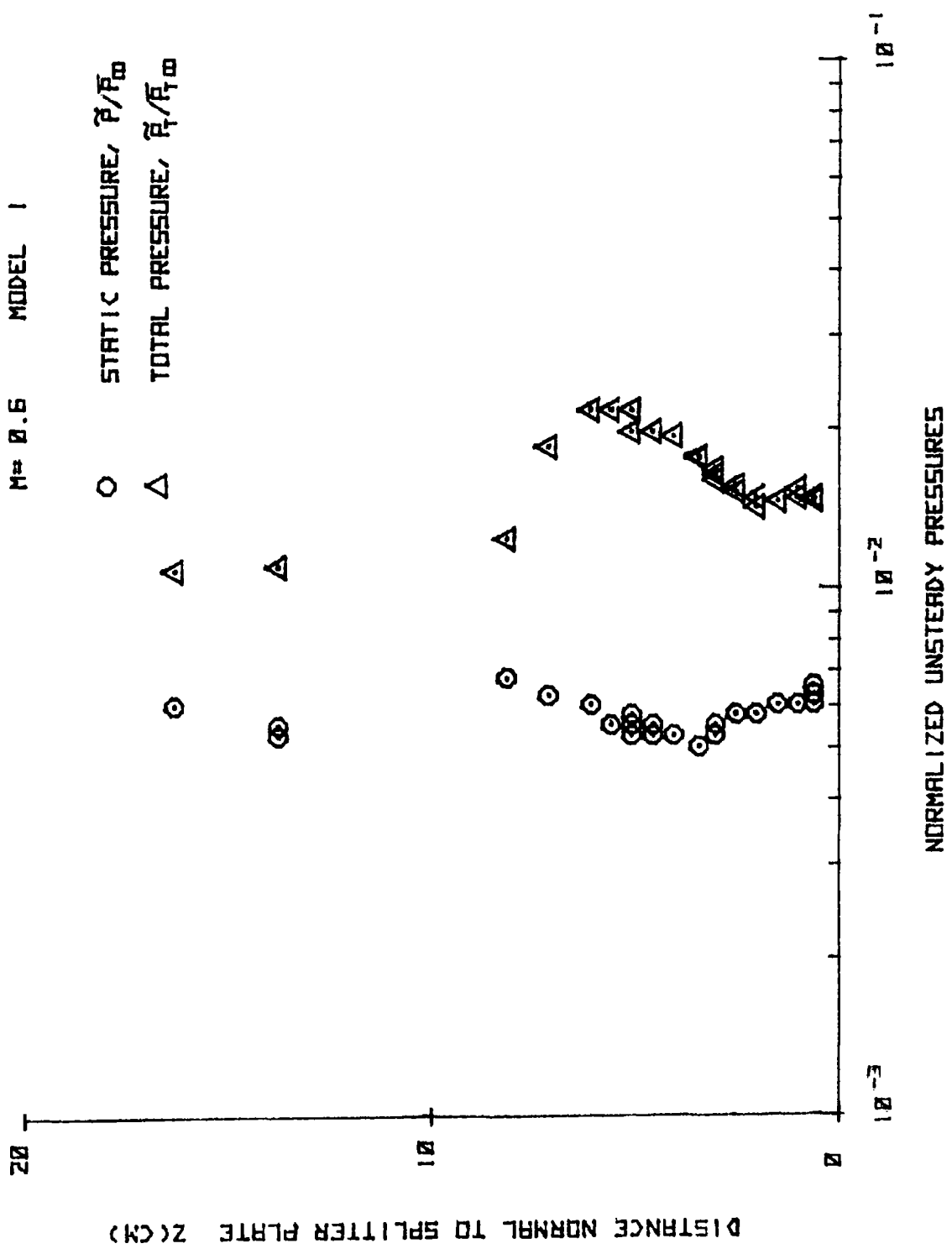


Figure 5(a). Normalized Unsteady Pressures for Model 1, $M_\infty=0.60$.

M= 0.89 MODEL 1

○ STATIC PRESSURE, \tilde{P}/\bar{P}_0
 △ TOTAL PRESSURE, \tilde{P}_t/\bar{P}_0

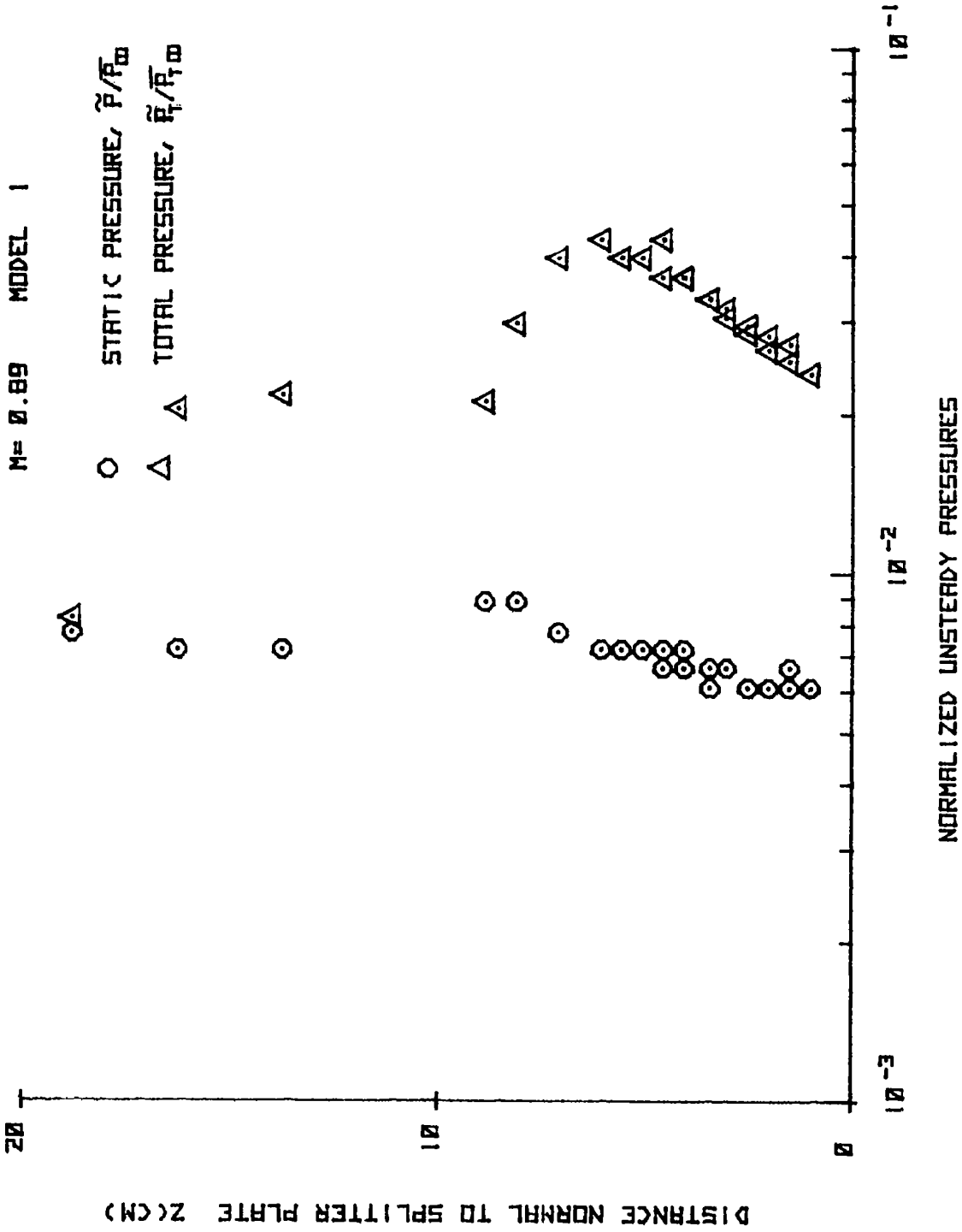


Figure 5(b). Normalized Unsteady Pressures for Model 1, $M_\infty = 0.89$.

M= 0.6 MODEL 2

○ STATIC PRESSURE, \bar{p}/\bar{p}_∞
△ TOTAL PRESSURE, \bar{p}_t/\bar{p}_∞

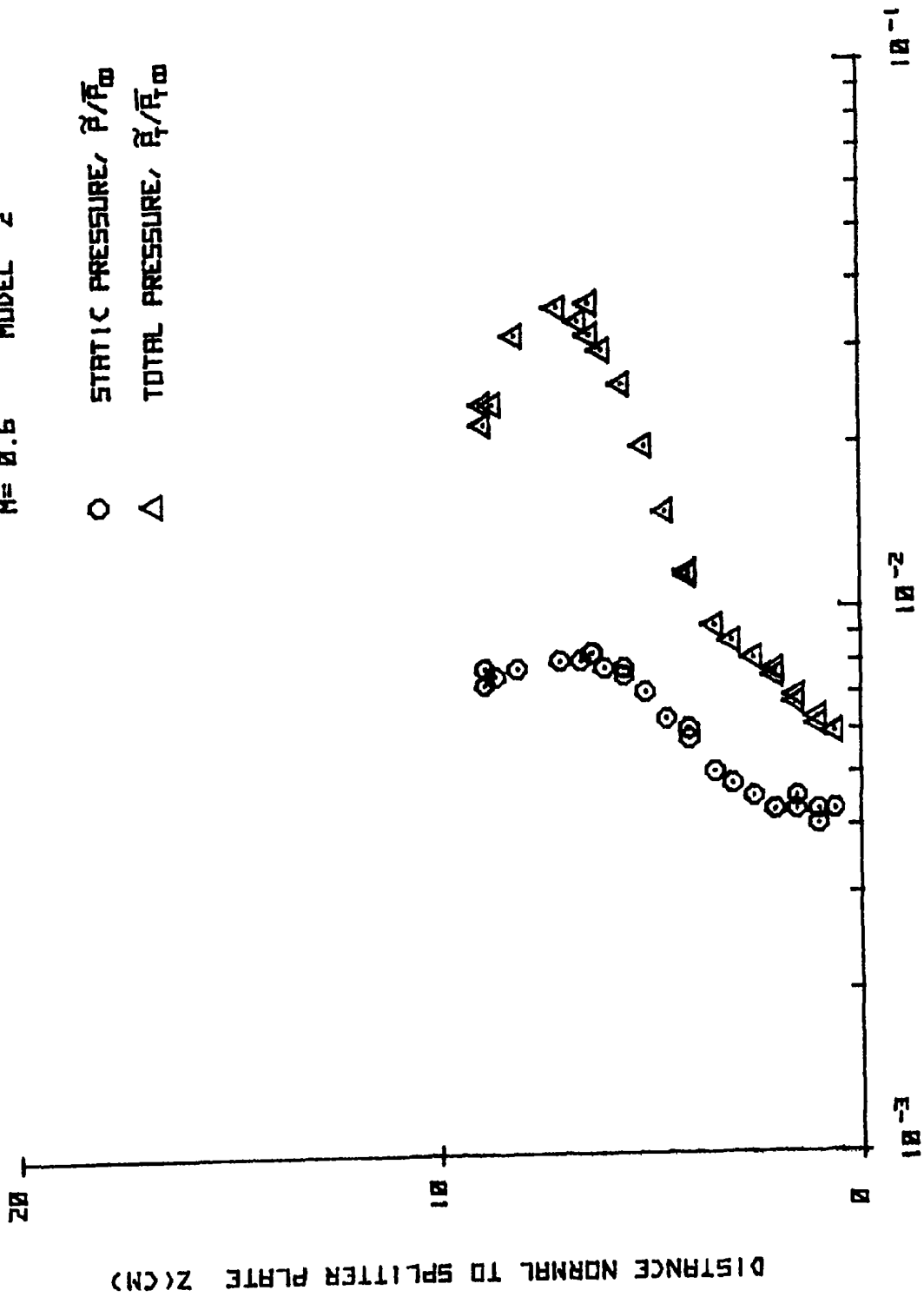


Figure 6(a). Normalized Unsteady Pressures for Model 2, $M_\infty=0.60$.

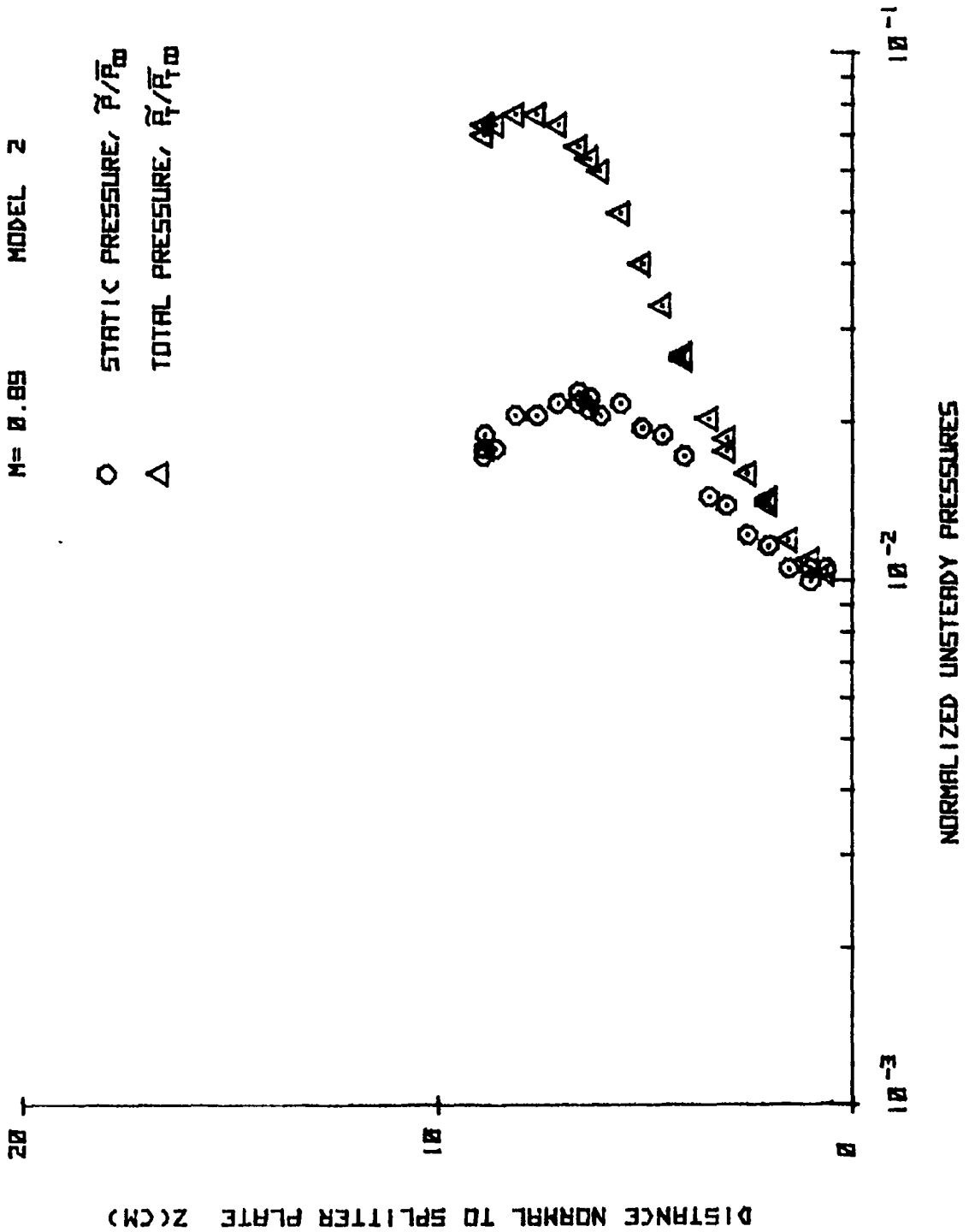


Figure 6(b). Normalized Unsteady Pressures for Model 2, $M_\infty=0.89$.

M = 0.6 MODEL 13

○ STATIC PRESSURE, \tilde{p}/\bar{p}_0
 △ TOTAL PRESSURE, \tilde{p}_t/\bar{p}_t^0

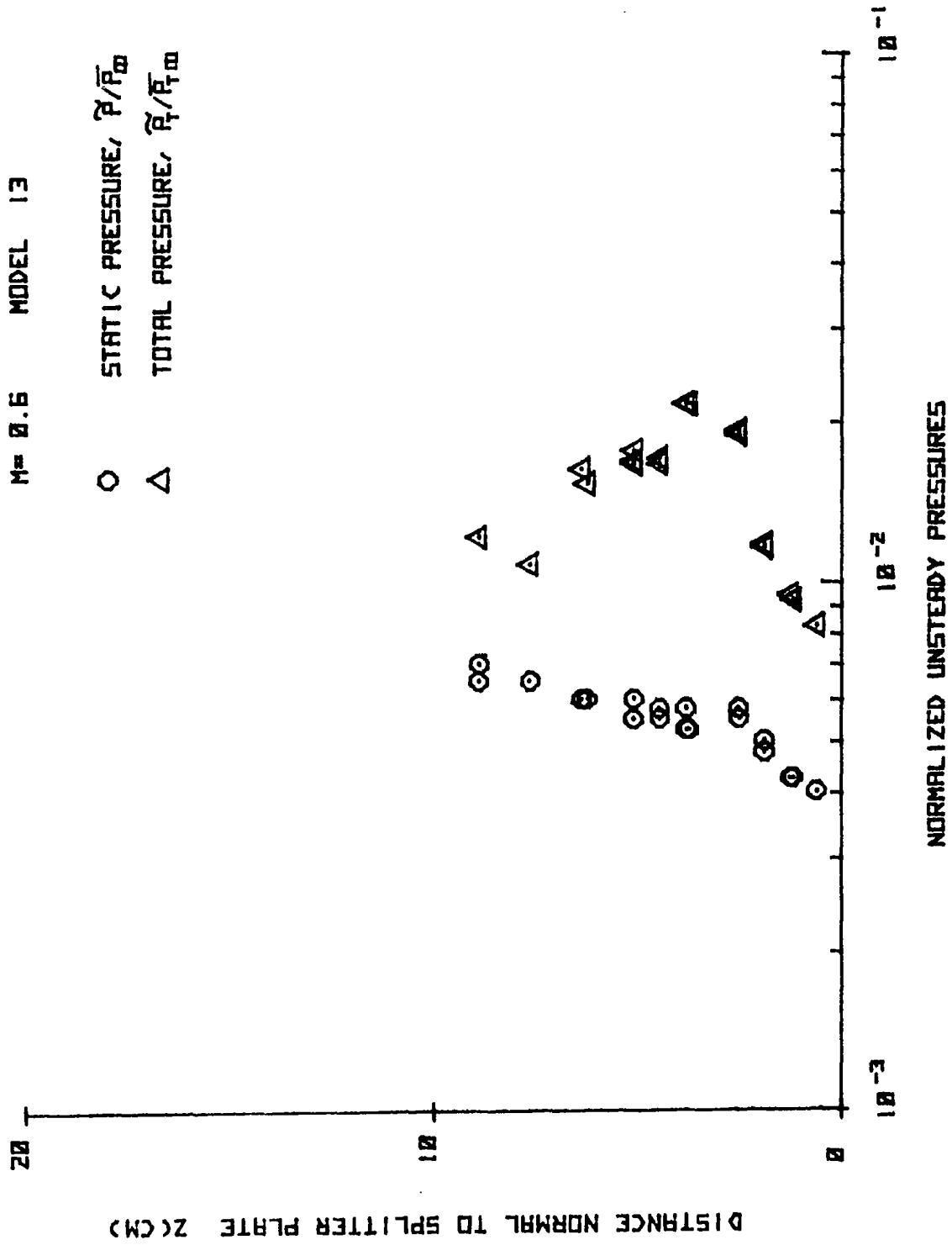


Figure 7(a). Normalized Unsteady Pressures for Model 13, $M_\infty = 0.60$.

M = 0.89 MODEL 13

○ STATIC PRESSURE, \tilde{p}/\bar{p}_0
 △ TOTAL PRESSURE, \tilde{p}_t/\bar{p}_0

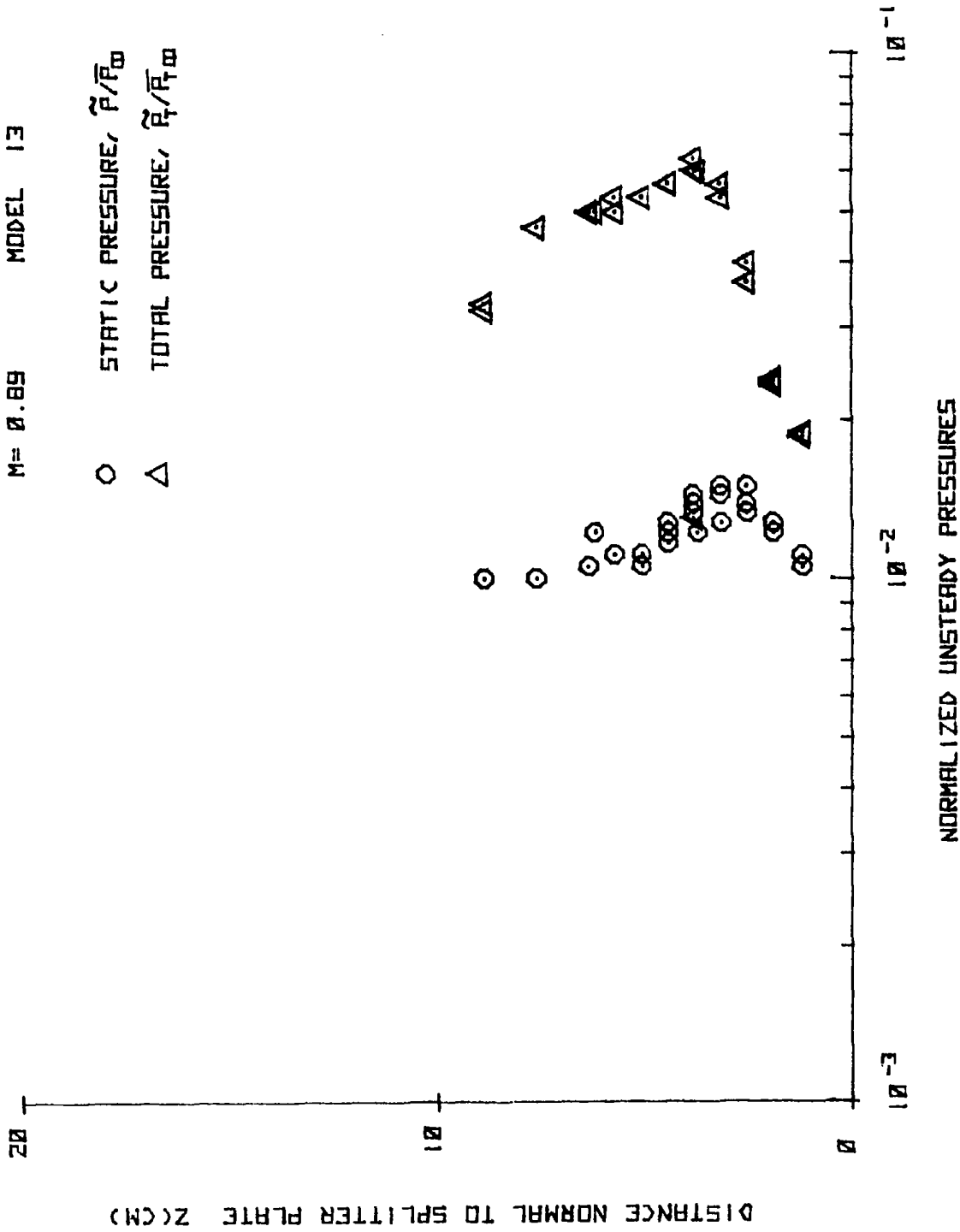


Figure 7(b). Normalized Unsteady Pressures for Model 13, $M_\infty = 0.89$.

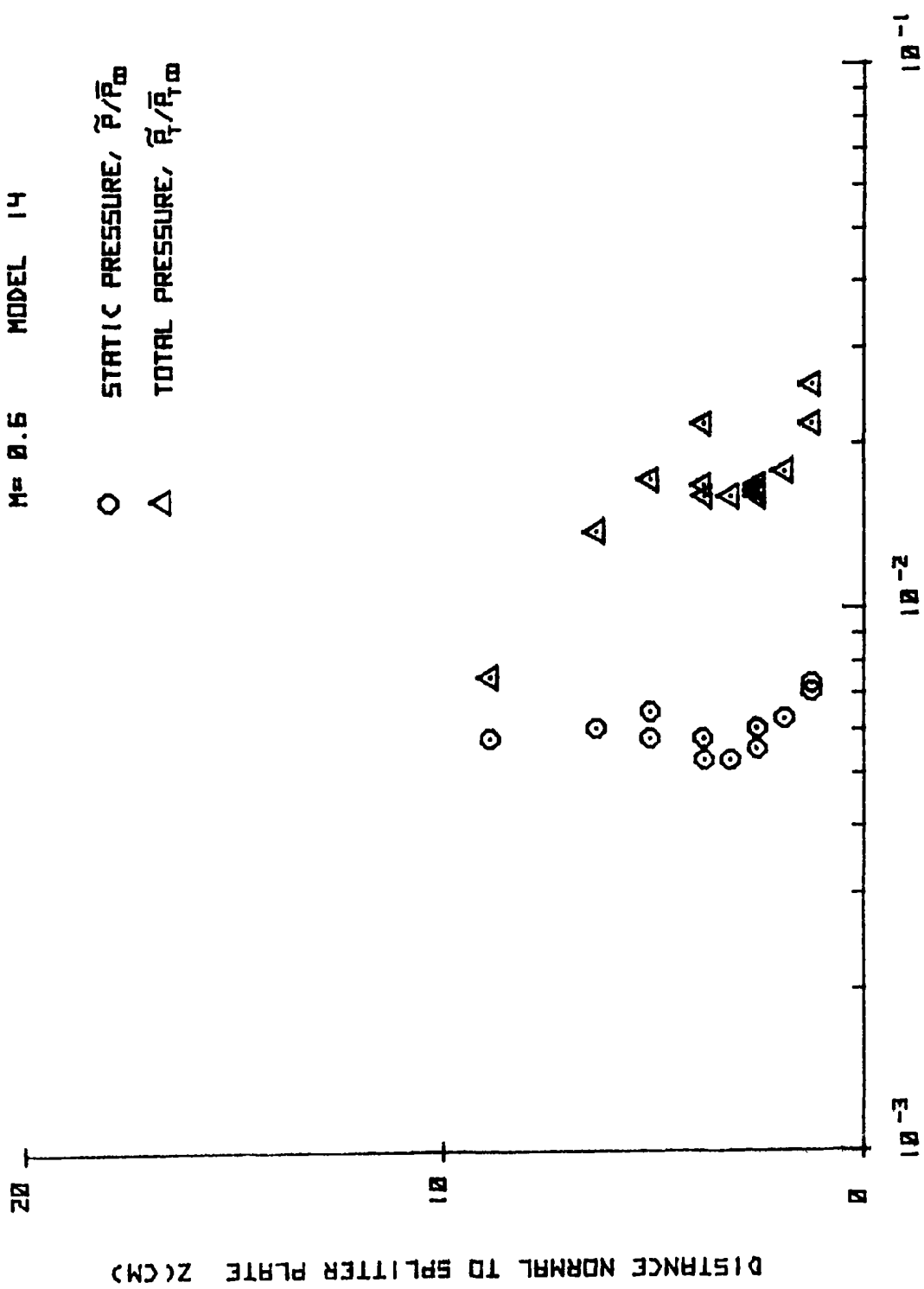


Figure 8(a). Normalized Unsteady Pressures for Model 14, $M_\infty = 0.60$.

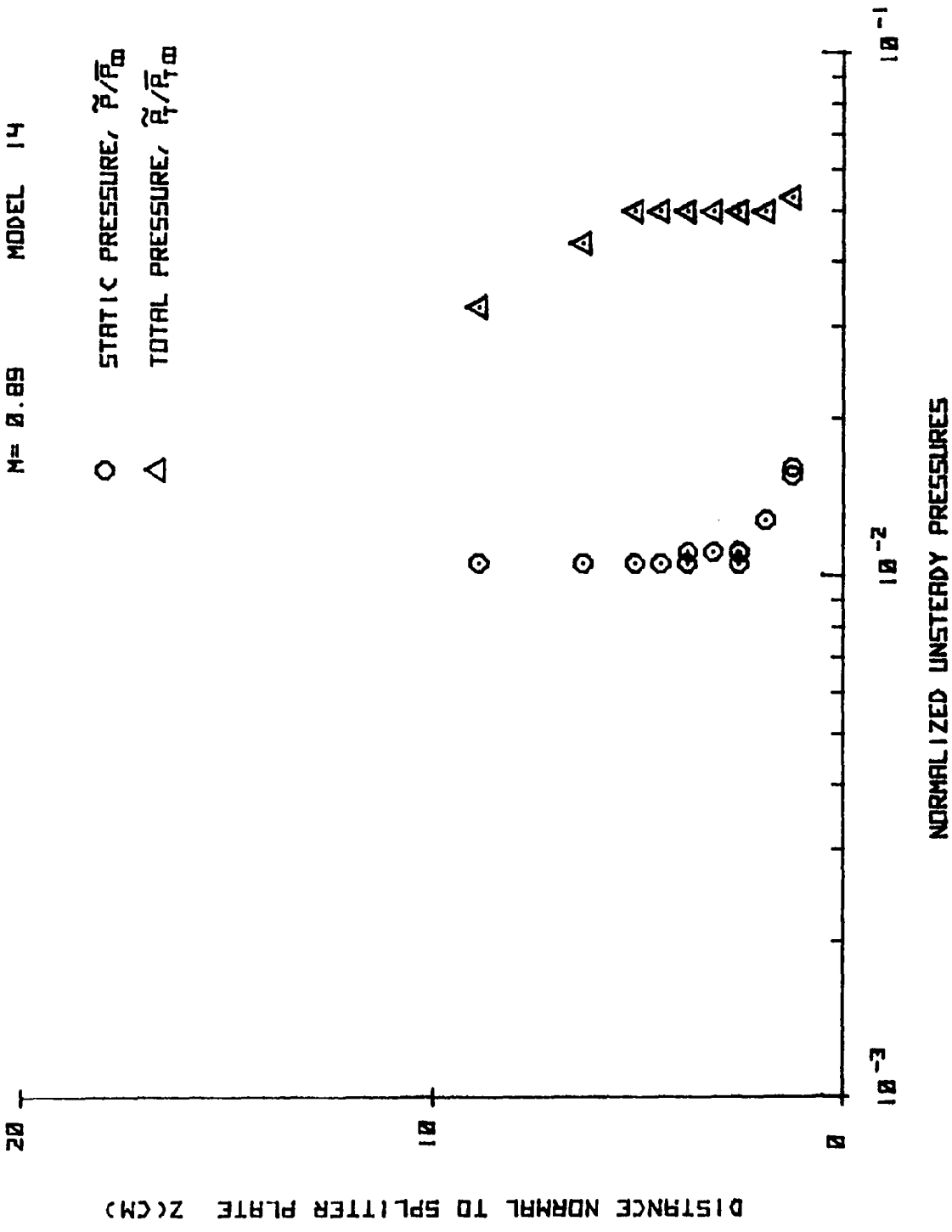


Figure 8(b). Normalized Unsteady Pressures for Model 14, $M_\infty = 0.89$

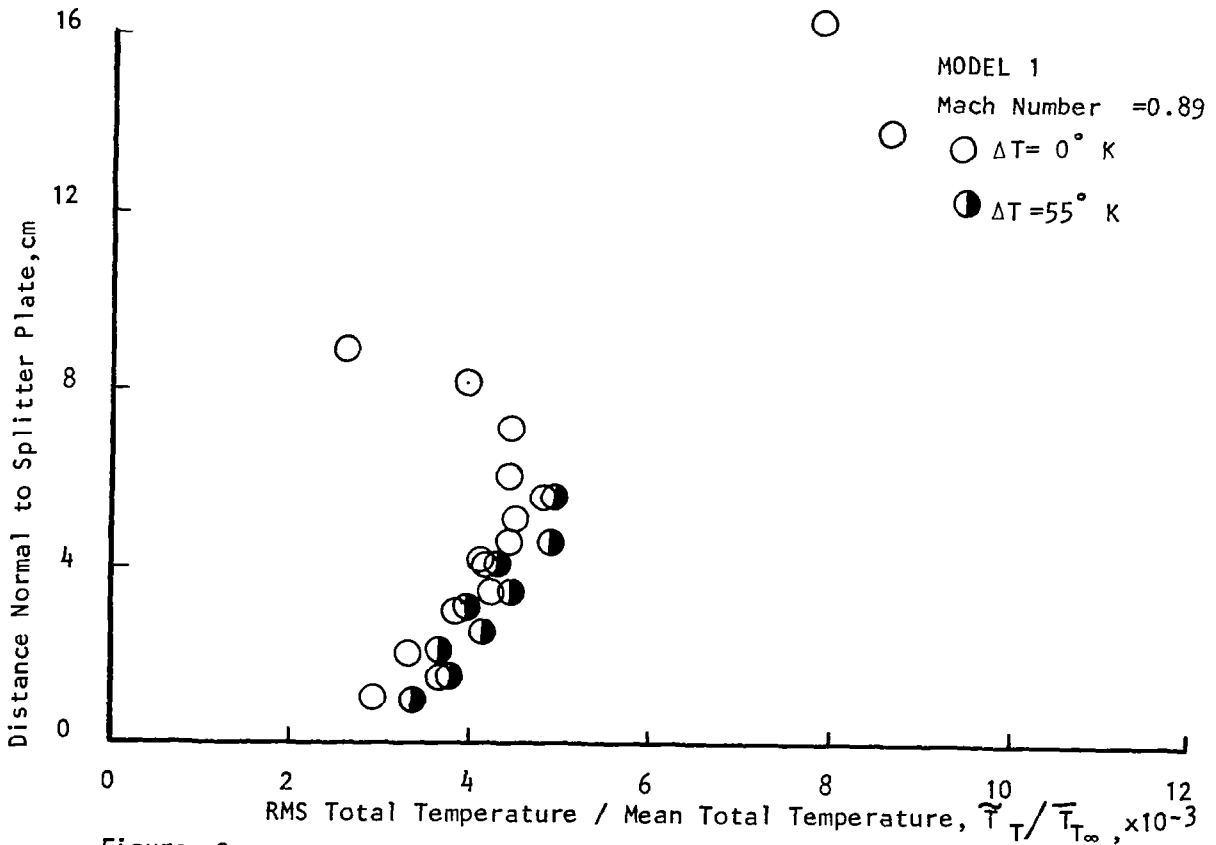
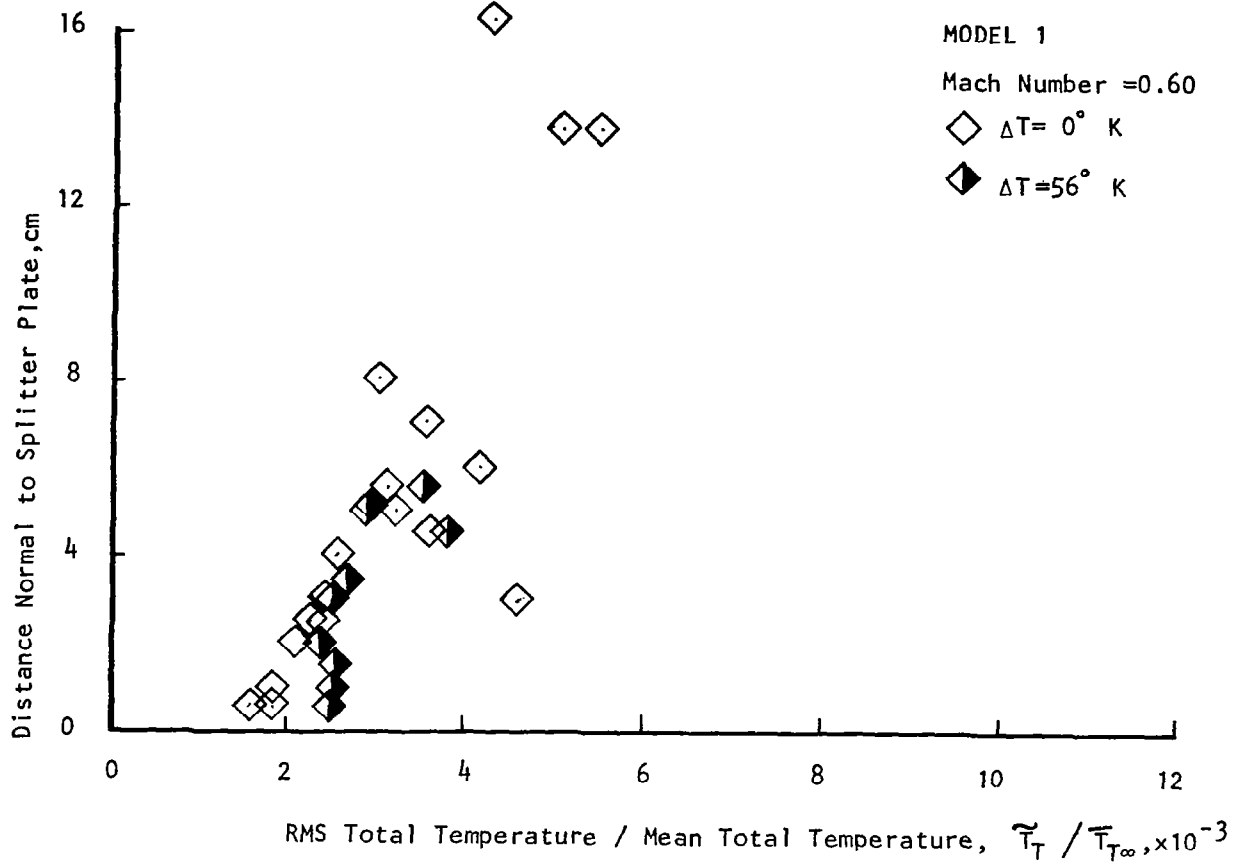


Figure 9 . Normalized Unsteady Total Temperatures for Model 1.

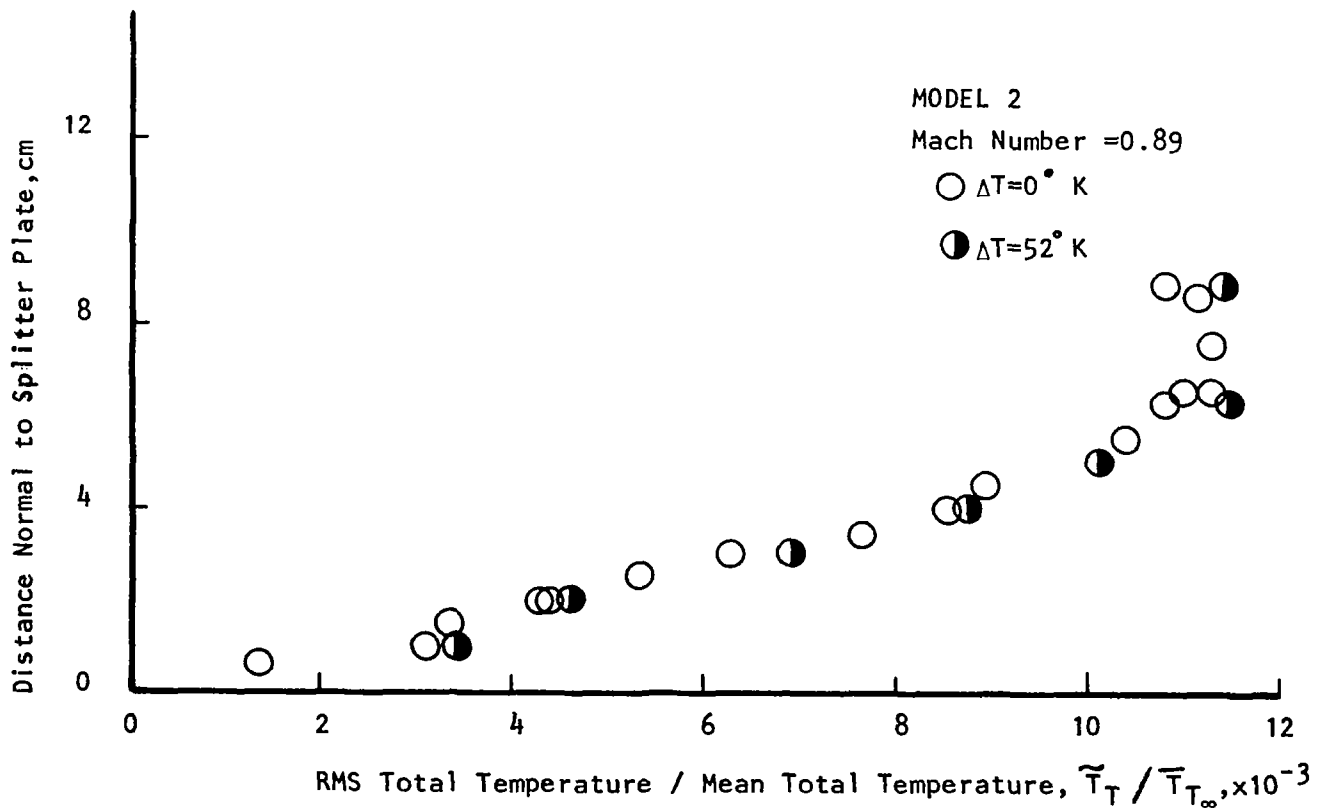
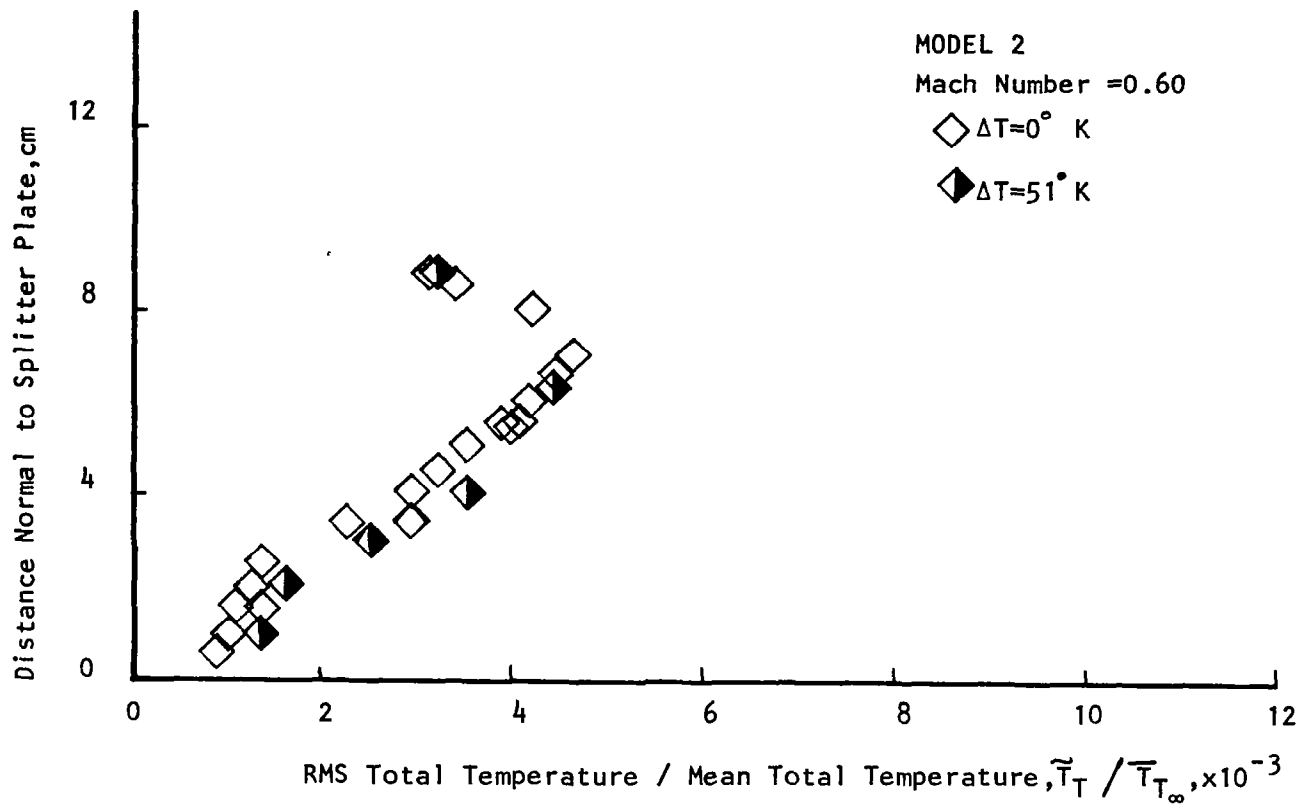


Figure 10 . Normalized Unsteady Total Temperatures for Model 2.

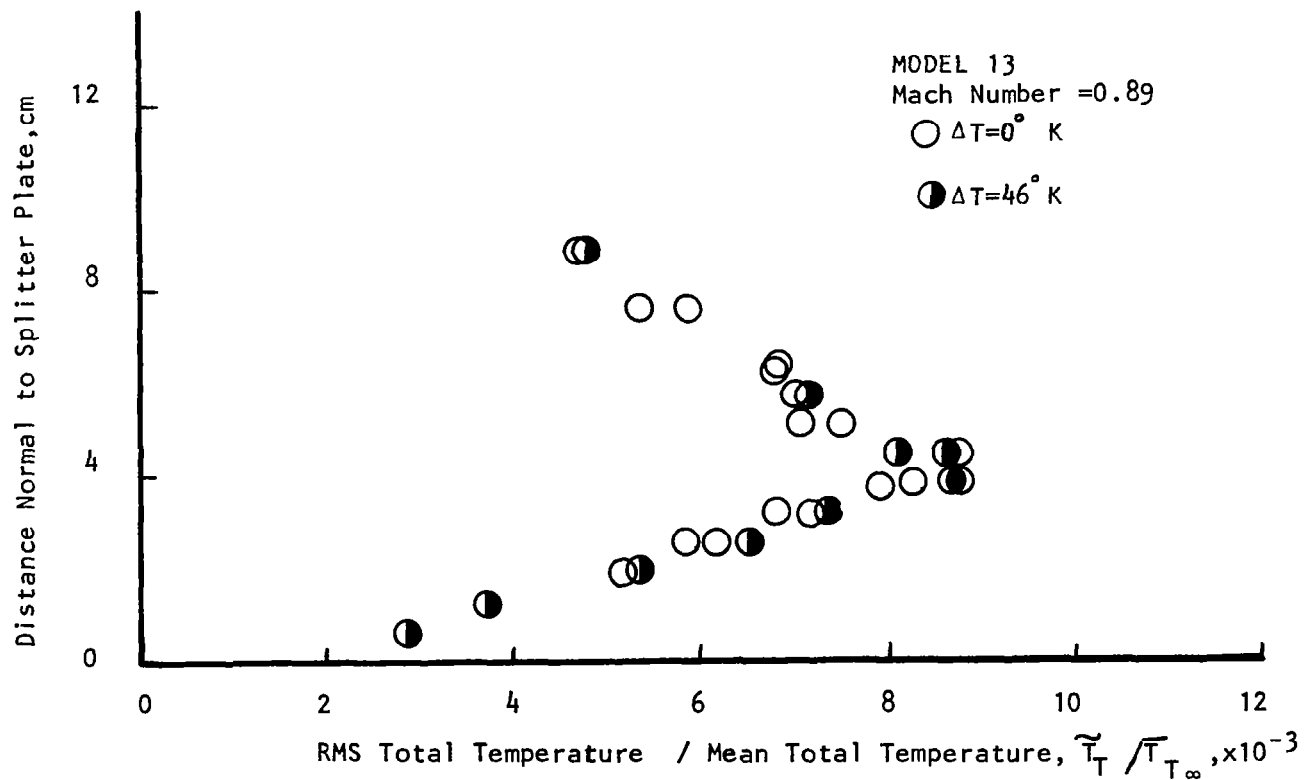
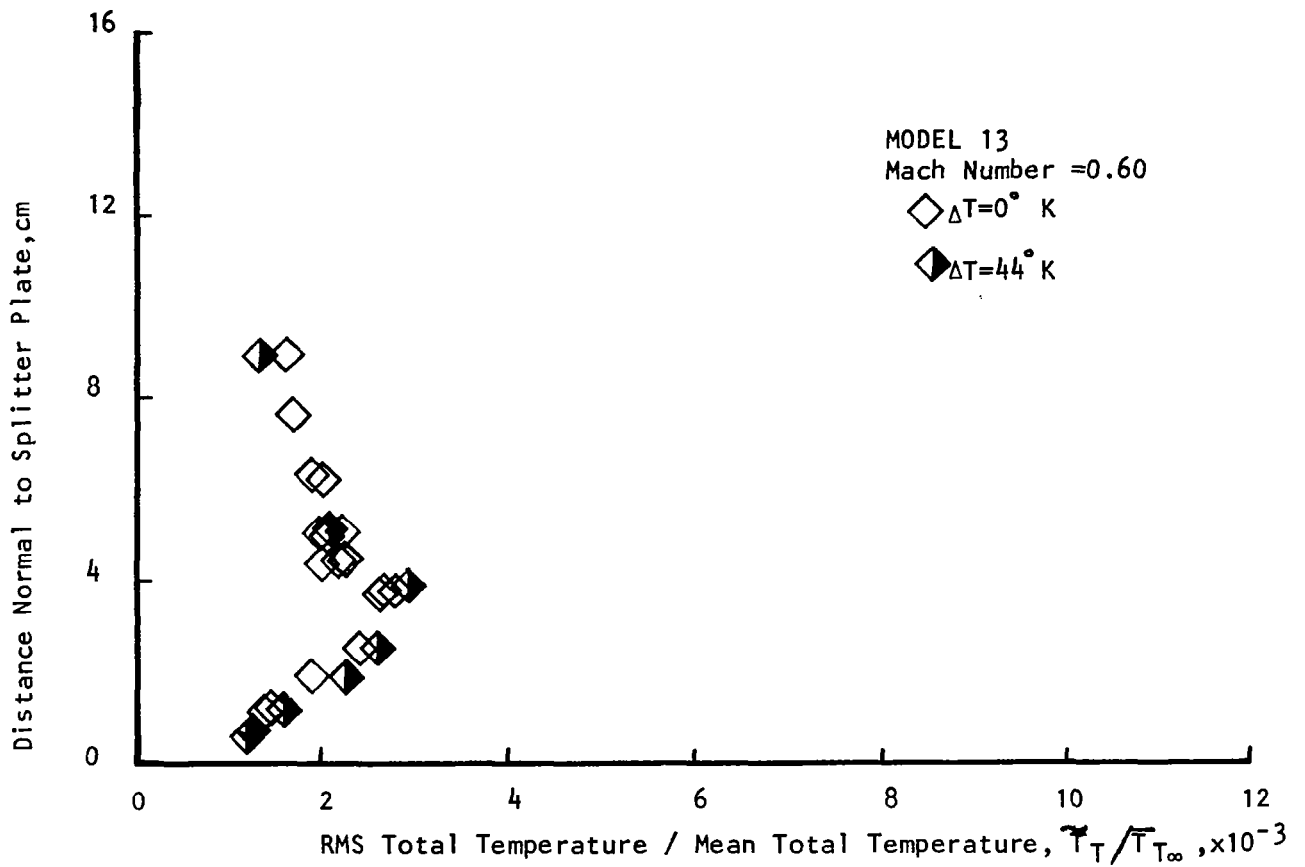


Figure 11. Normalized Unsteady Total Temperatures for Model 13.

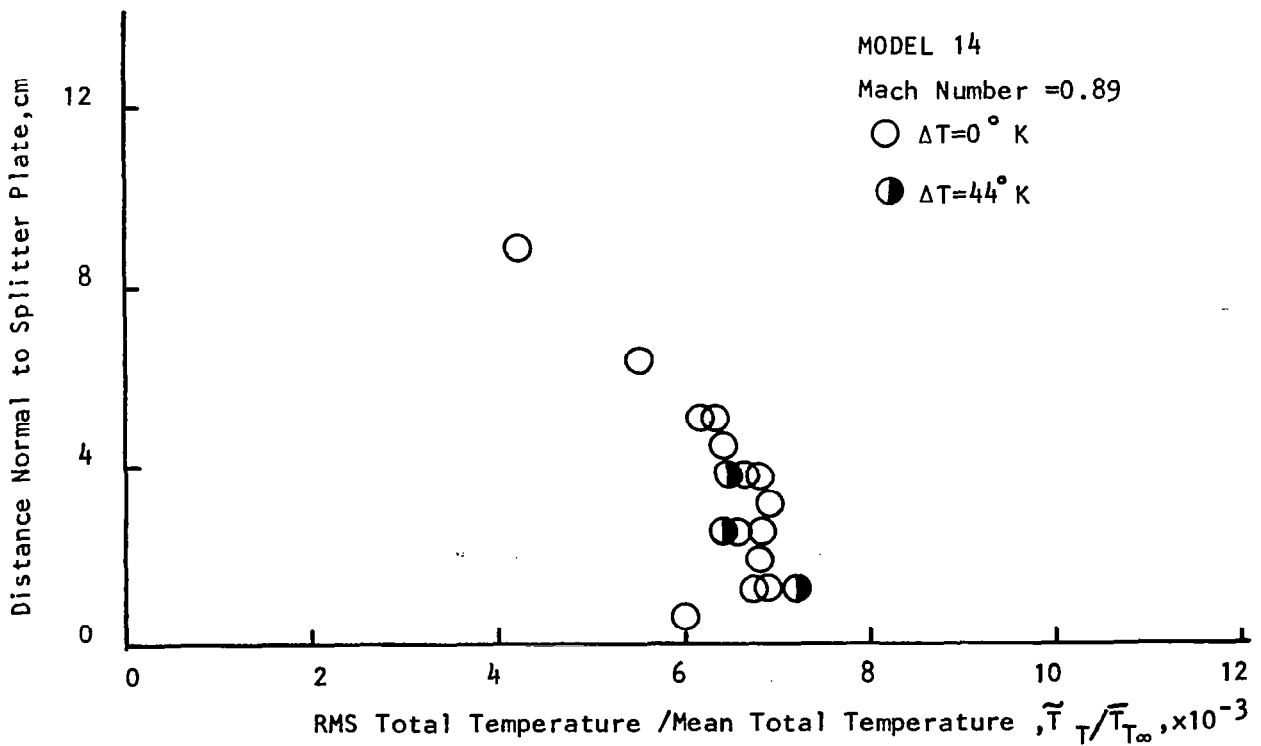
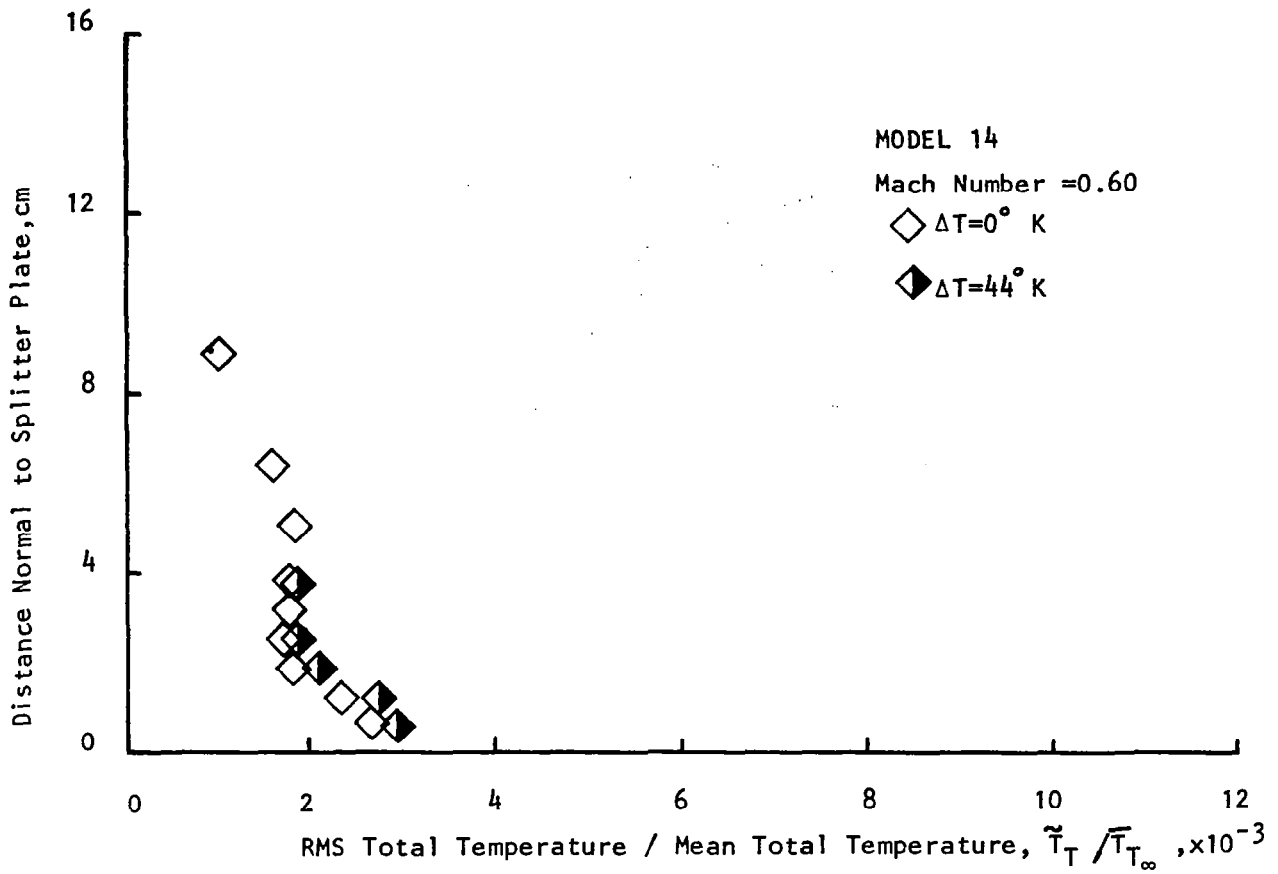


Figure 12. Normalized Unsteady Total Temperatures for Model 14.

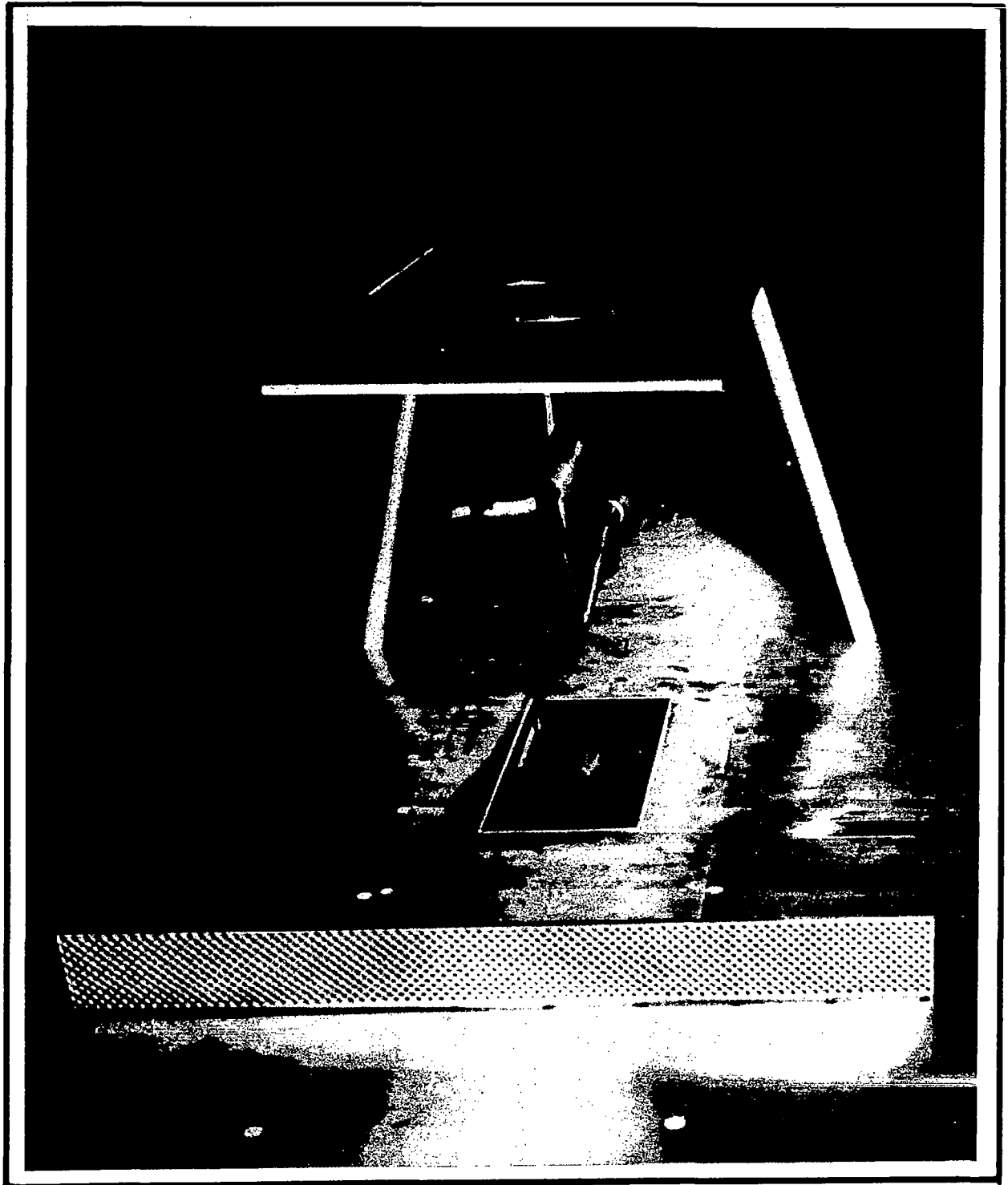


Figure 13 . Two Multi-probes in the Test Section for Correlation Measurements .

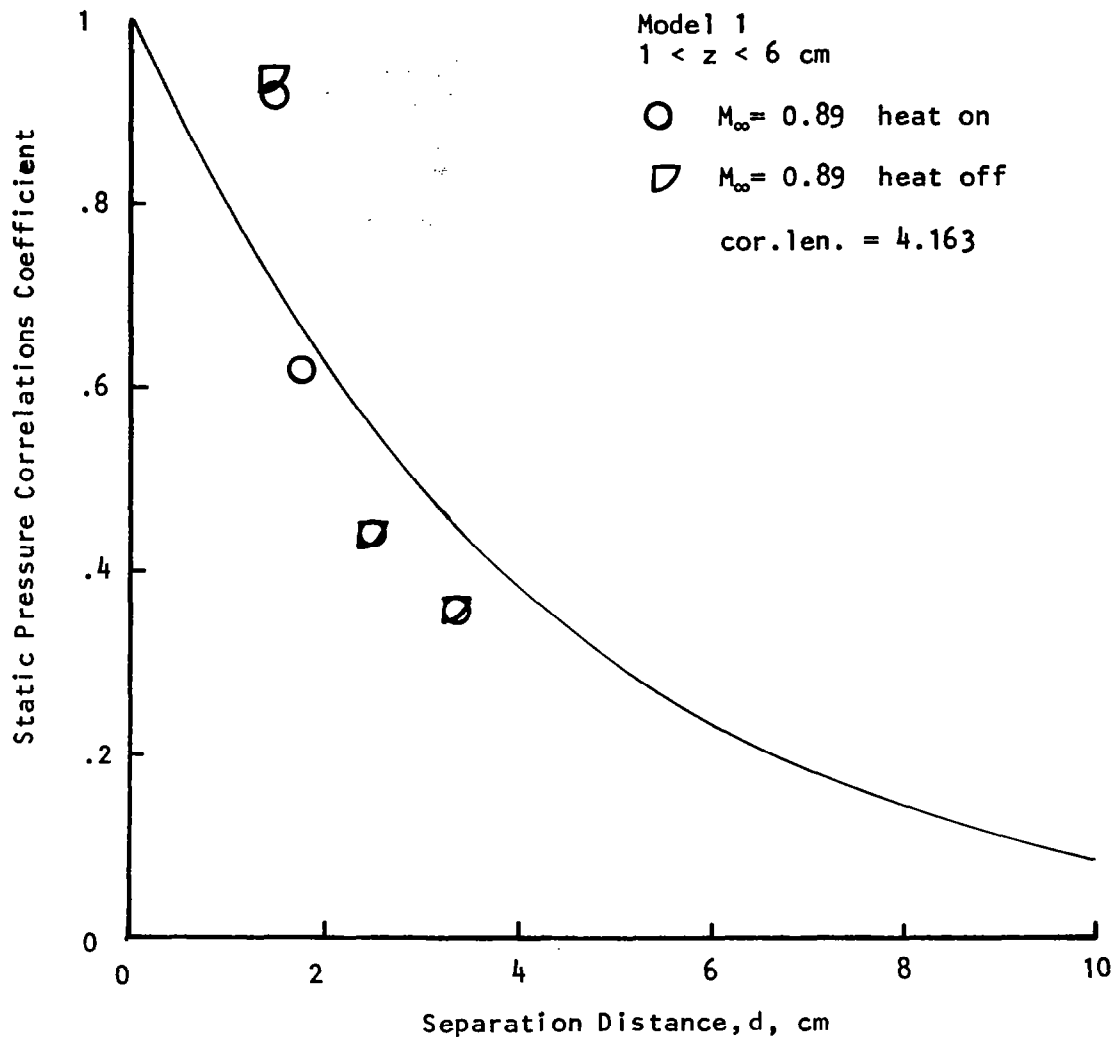


Figure 14(a). Static Pressure Correlation Coefficient versus Separation Distance for Model 1.

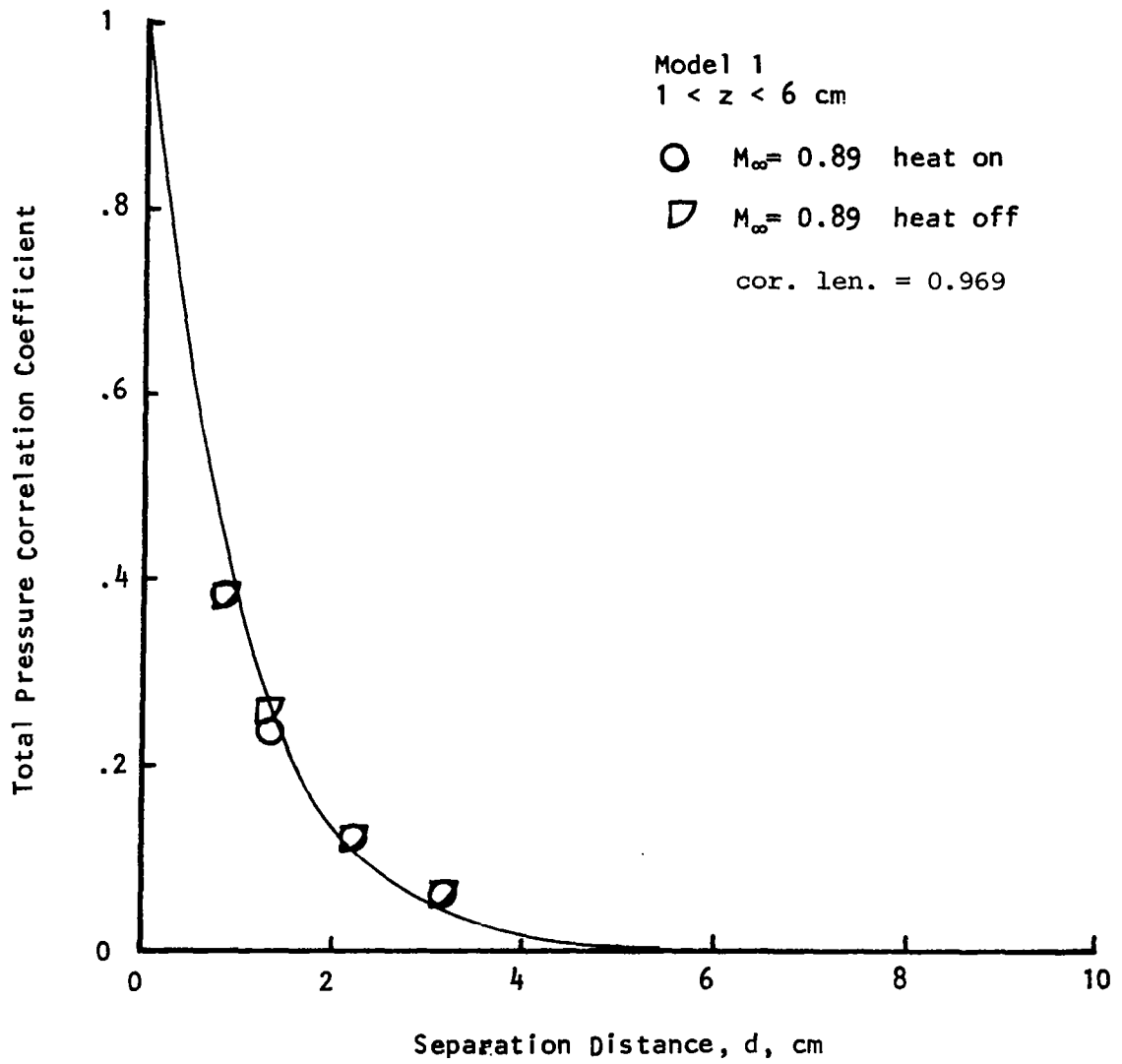


Figure 14(b). Total Pressure Correlation Coefficient versus Separation Distance for Model 1.

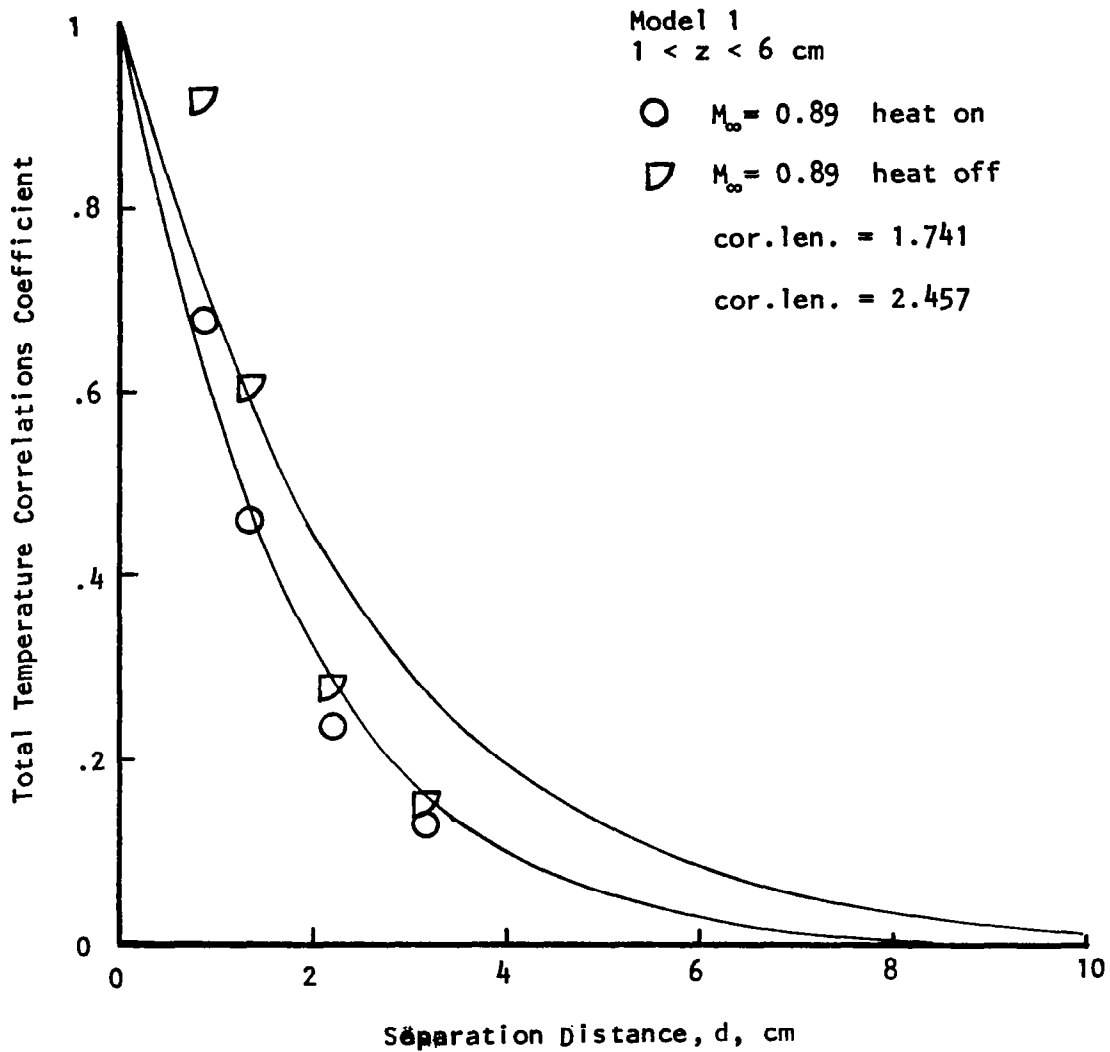


Figure 14(c). Total Temperature Correlation Coefficient versus Separation Distance for Model 1.

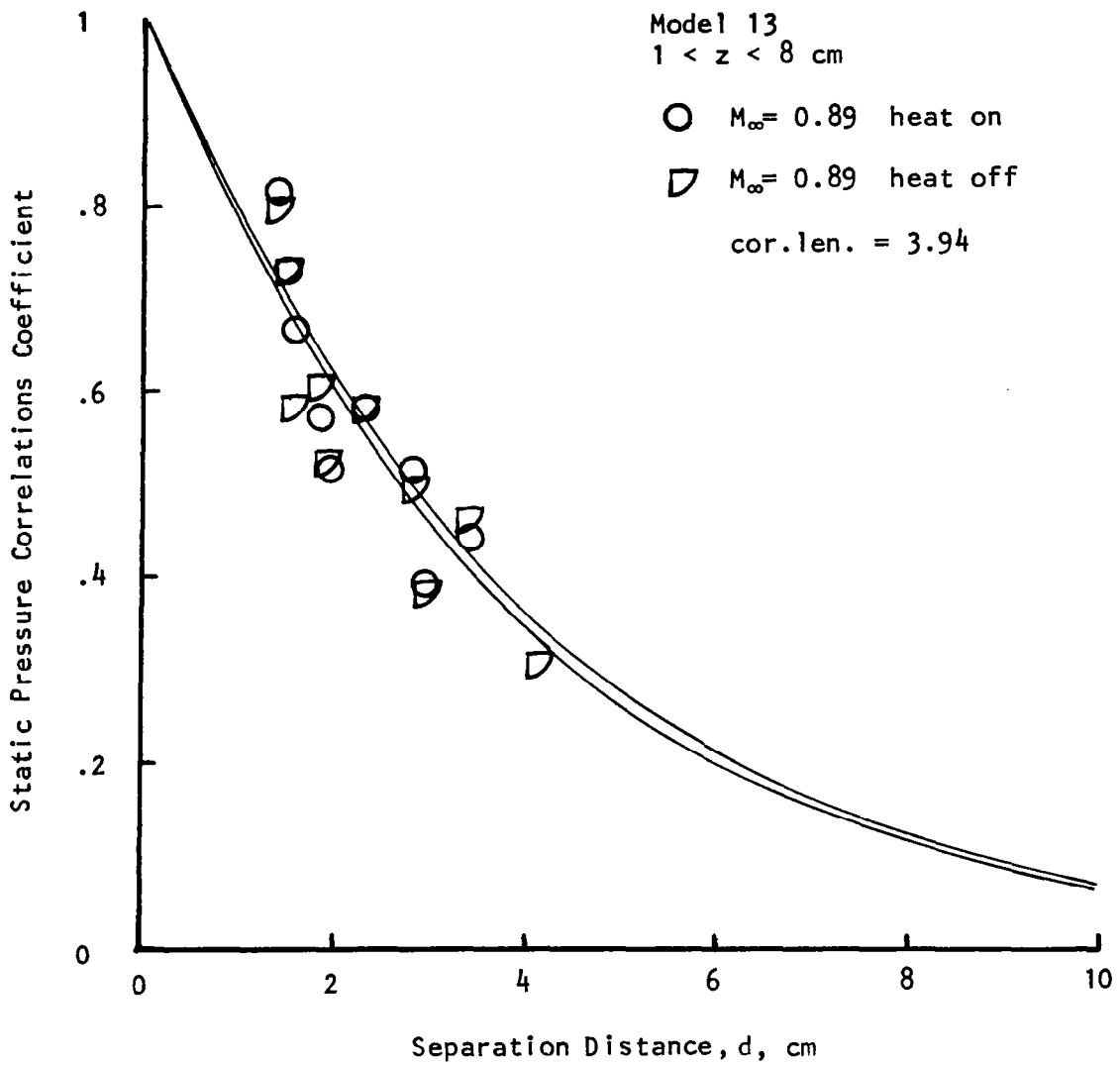


Figure 15(a). Static Pressure Correlation Coefficient versus Separation Distance for Model 13.

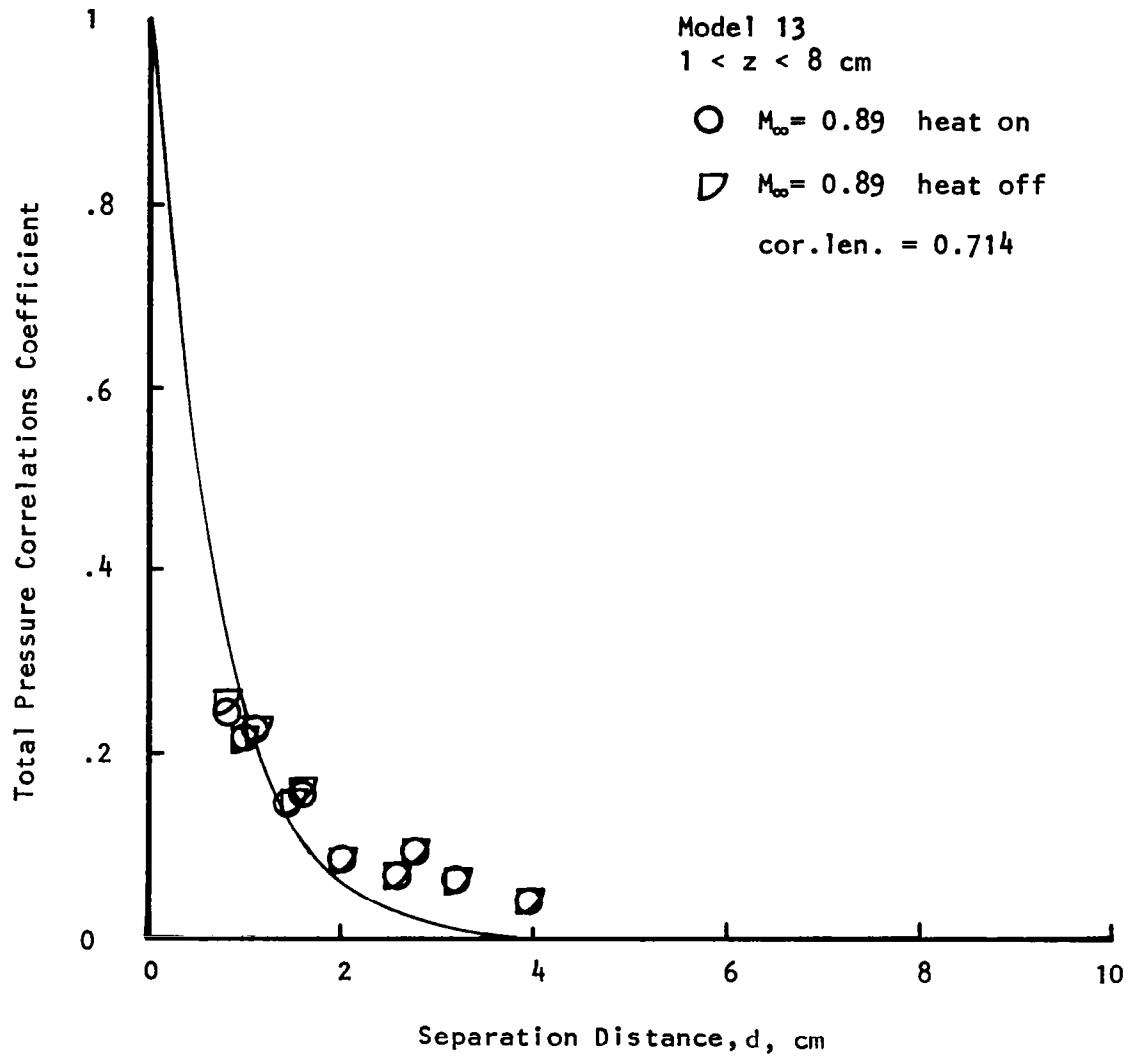


Figure 15(b). Total Pressure Correlation Coefficient versus Separation Distance for Model 13.

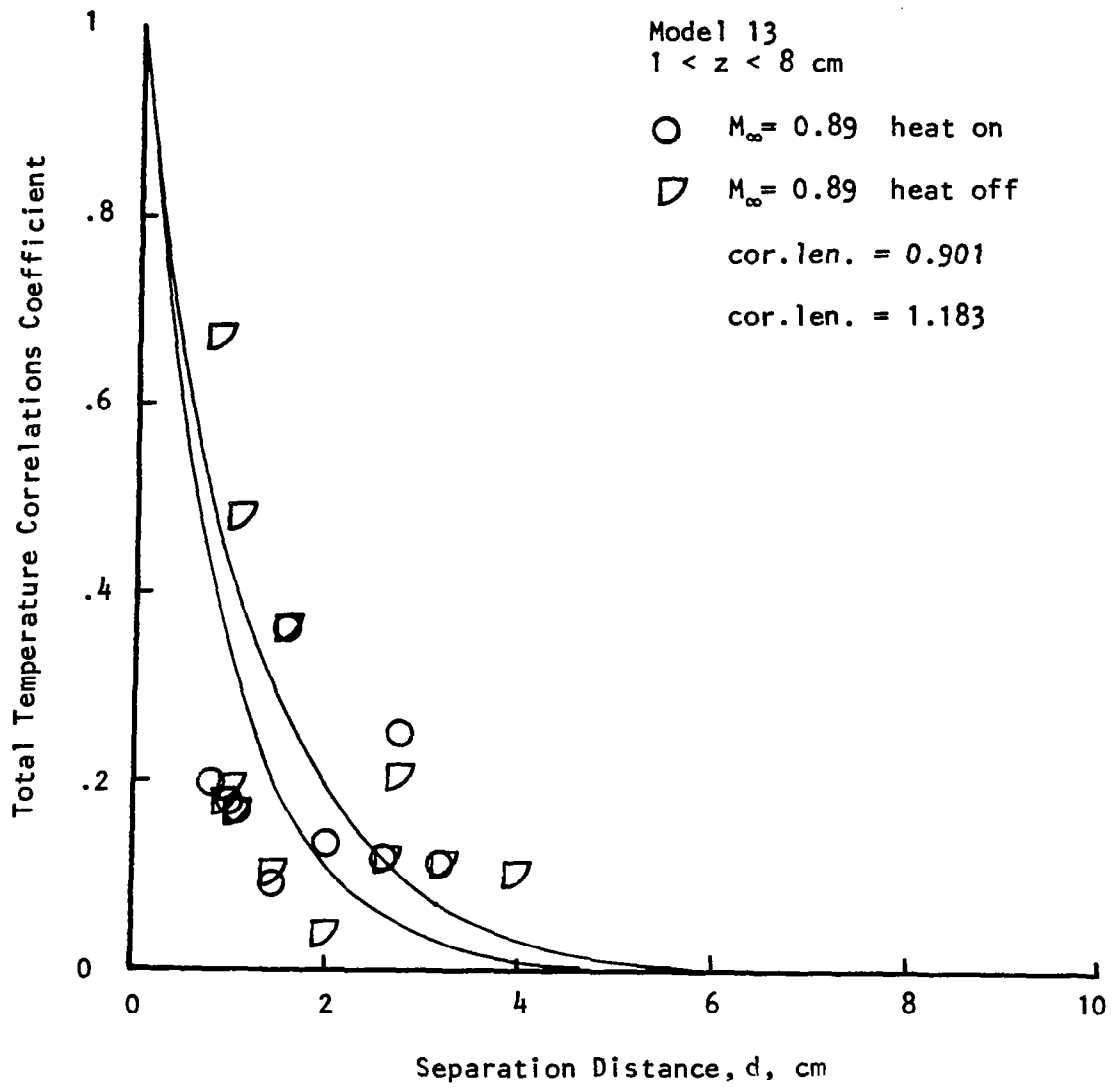


Figure 15 (c). Total Temperature Correlation Coefficient versus Separation Distance for Model 13.

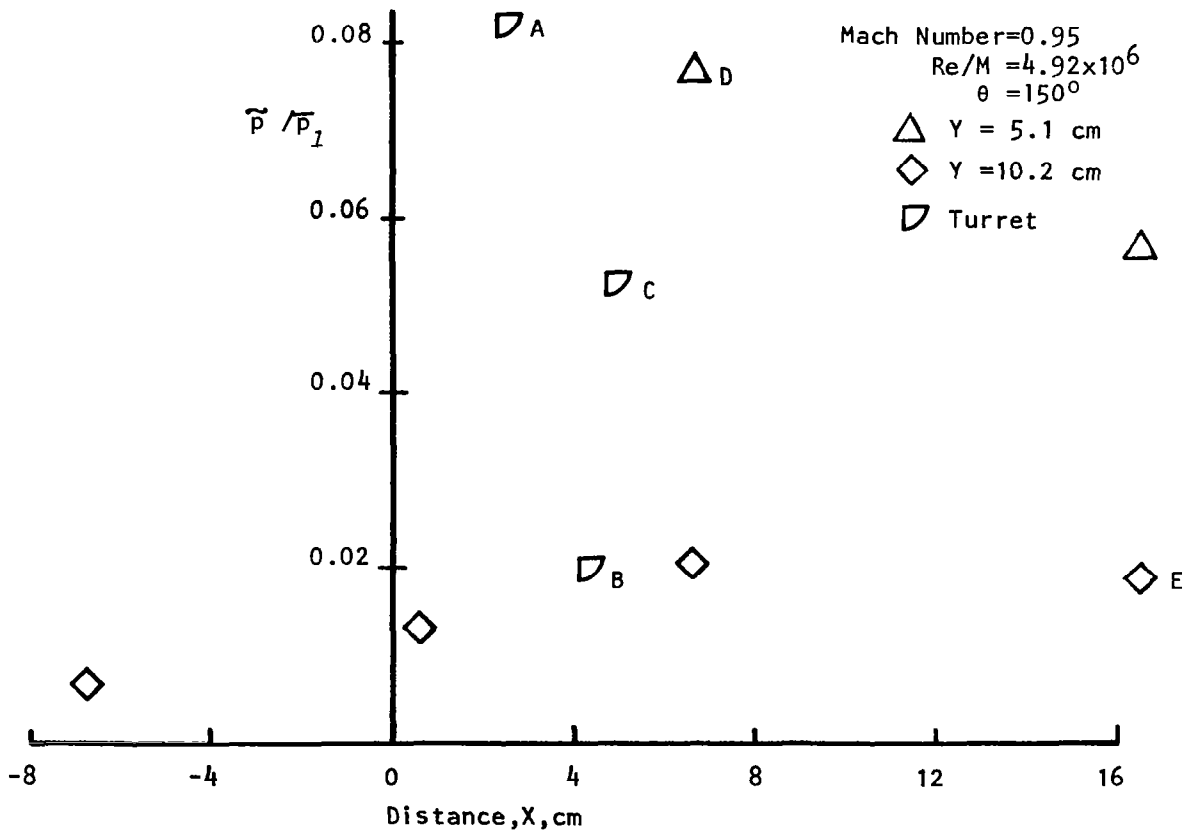
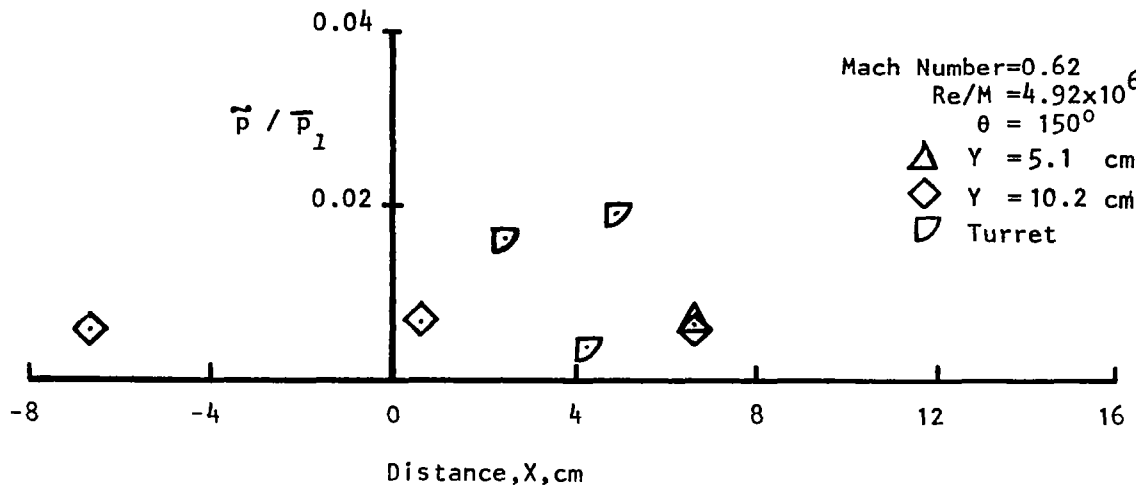
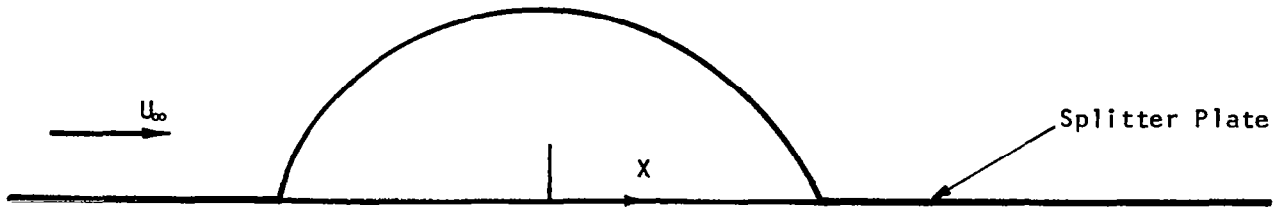


Figure 16. Normalized Unsteady Static Pressures on Coelostat Turret Model.

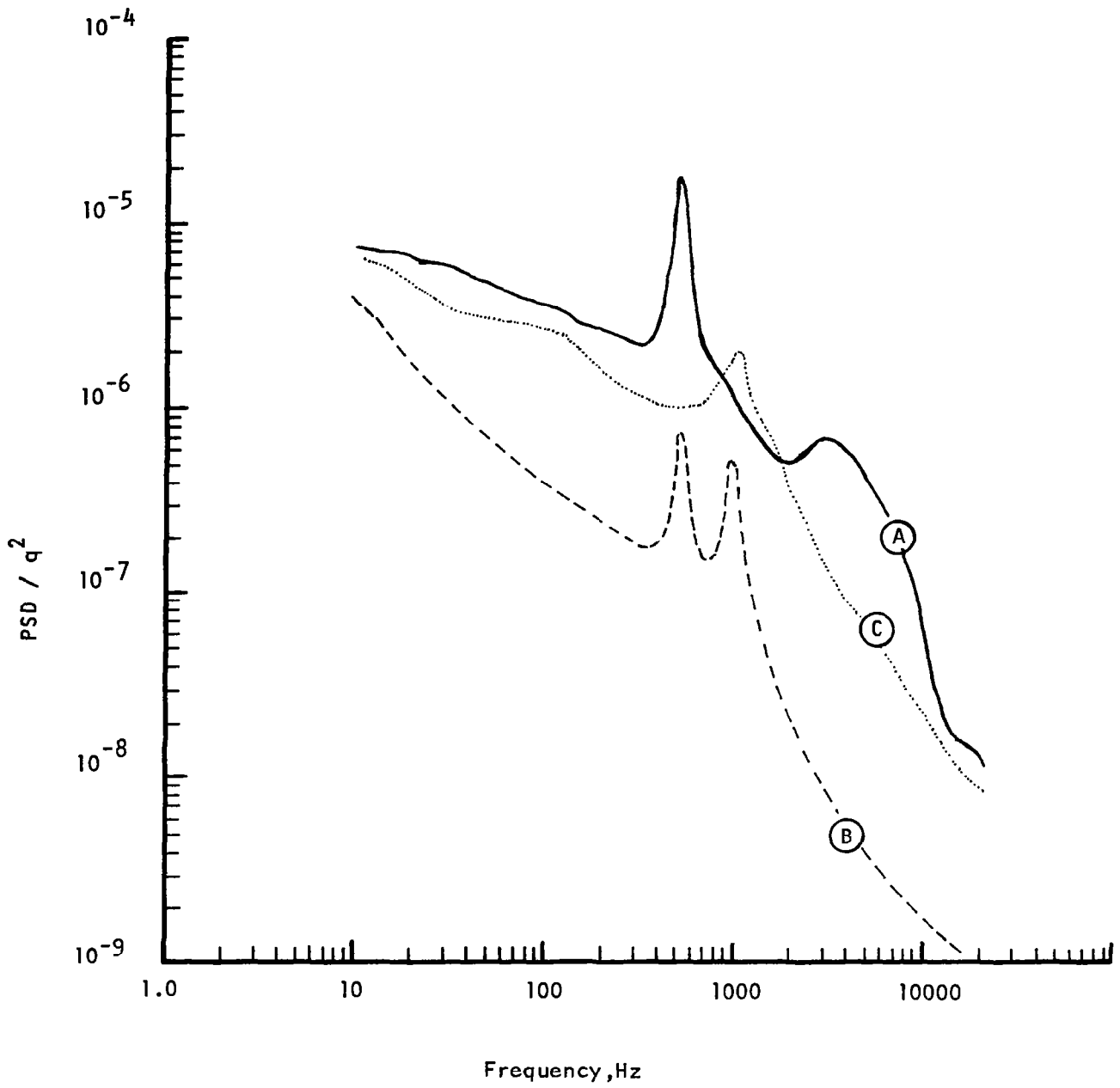


Figure 17. Power Spectral Density of Pressures from the Coelostat Turret Model Tests.

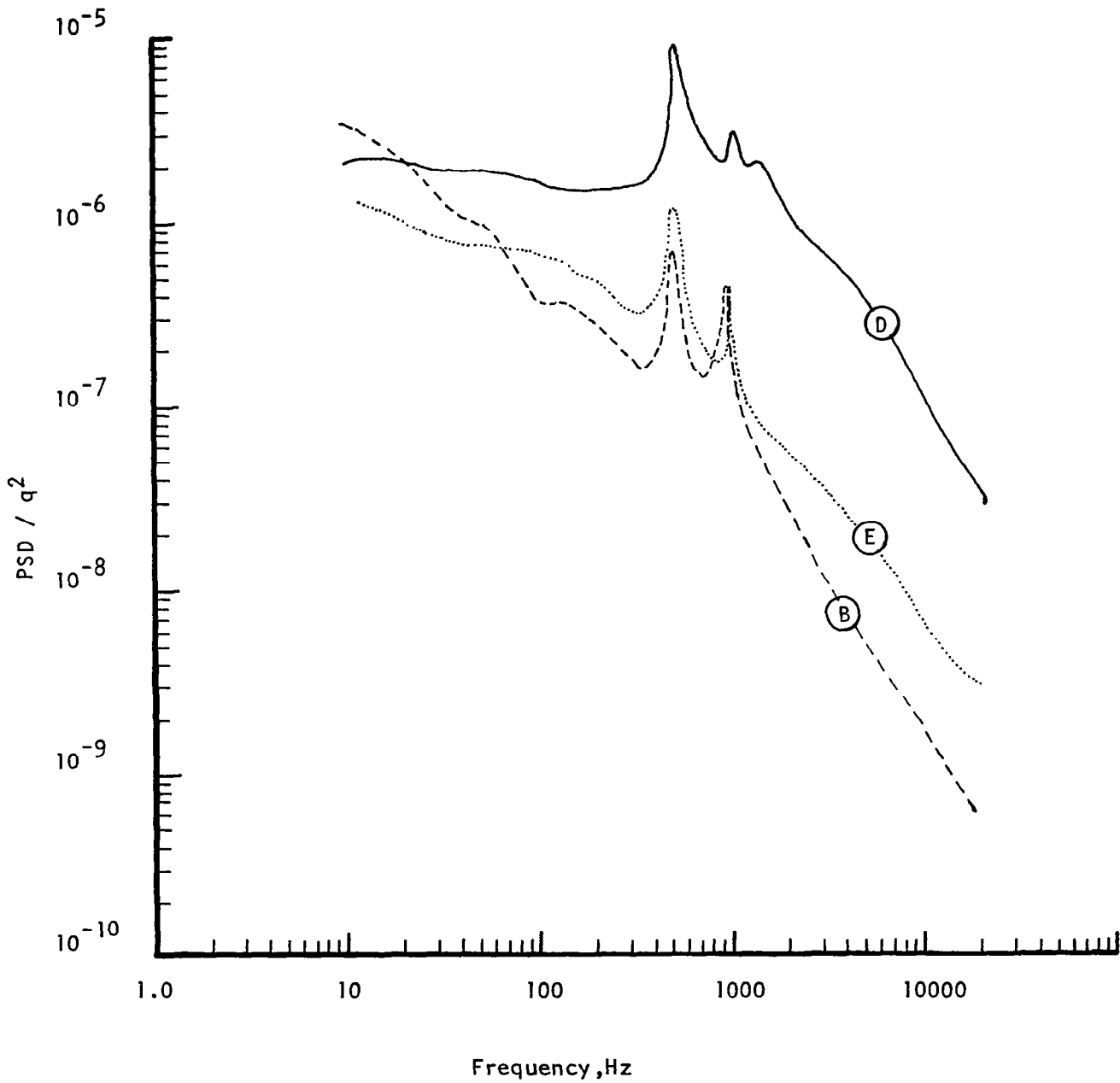


Figure 18. Power Spectral Density of Pressures from the Coelostat Turret Model Tests.